Single crystal investigation, spectroscopic, DFT studies, and *in-silico* molecular docking of the anticancer activities of acetylacetone coordinated Re(I) tricarbonyl complexes

Amanda-Lee E. Manicum [a*], Hitler Louis [b,c], Gideon E. Mathias [b,c], Ernest C. Agwamba [b,d], Frederick P. Malan[e], Tomsmith O. Unimuke [b,c], Wakopo J. Nzondomyo[a], Sibusiso A. Sithole[a], Supratim Biswas[f] and Sharon Prince[f]

[a] Department of Chemistry, Tshwane University of Technology, P.O. Box X680, Pretoria, 0001, South Africa
[b] Computational and Bio-Simulation Research Group, University of Calabar, Calabar, Nigeria
[c] Department of Pure and Applied Chemistry, Faculty of Physical Sciences, University of Calabar, Calabar, Nigeria
[d] Department of Chemical Sciences, Clifford University, Owerrinta, Nigeria
[e] Department of Chemistry, University of Pretoria, 02 Lynnwood Road, Hatfield, Pretoria 0001, South Africa
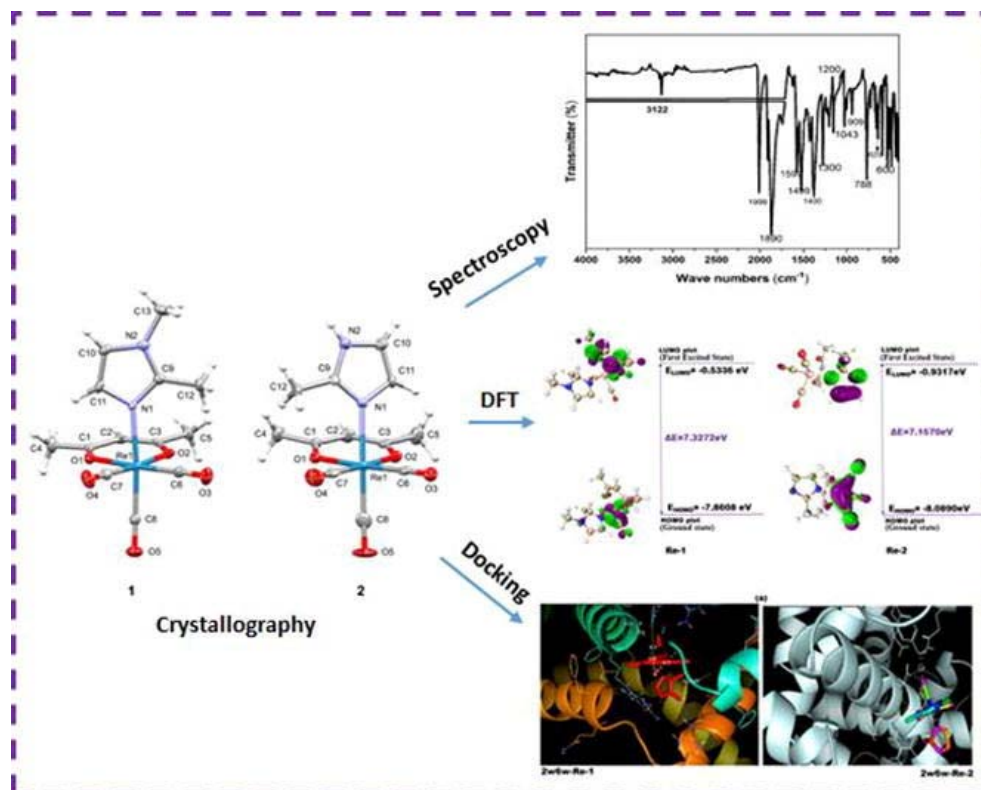[f] Department of Human Biology, University of Cape Town, Anzio Road Observatory 7925, Cape Town, South Africa

*Corresponding author email address: AE Manicum (ManicumAE@tut.ac.za)

Abstract

Acetylacetone was used in the synthesis of the neutral complexes, *fac*-[Re(Acac)(CO)$_3$(1,2-DiCH$_3$Im)] (**Re-1**) and *fac*-[Re(Acac)(CO)$_3$(2-CH$_3$Im)] (**Re-2**), incorporating the (2 + 1) mixed ligand approach. The synthesized complexes were characterized by FT-IR, NMR, UV/Vis, and XRD. In addition, two new Re(I) tricarbonyl crystal structures (**Re-1**) and (**Re-2**) are reported, presenting distorted octahedral coordination of the ligands around the metal center. The spectroscopic, molecular properties, and molecular docking of the synthesized compounds as potential anticancer drug was investigated. Before characterization, the theoretical investigation was carried out using M062X-D3, ωB97XD, and PBE0-D3 methods with Gen and def2-SVP basis set. The binding score obtained upon docking both ligands against the 2w6w receptor is -6.8kcal/mol and -6.9kcal/mol respectively. Interestingly when both ligands were docked against the 5w9d receptor, it appears that the **Re-1** drug bind more with a binding affinity of -6.7kcal/mol while the **Re-2** ligand was observed to have a binding score of -6.5kcal/mol.

Graphical abstract

1.   Introduction

Despite the growing extent of research, cancer continues to be one of the world's most prevalent causes of death, especially in high-income nations (although cancer rates are rising in low-income nations, which already account for 75% of cancer deaths globally). The type and stage of the tumour, as well as the patient's age, sex, and socioeconomic status, all have a significant impact on the survival rates [1]. For instance, it is predicted that half of adult cancer patients in England and Wales (15–90 years old) who were diagnosed in 2010–2011 will not live for another 10 years or longer [2]. Cancer treatment is based on the kind, stage, and location of the tumour, although the majority of patients receive chemotherapy as the primary therapy or in conjunction with radiotherapy, surgery, or both. Platinum-based medications (cisplatin, carboplatin, and oxaliplatin) are used to treat more than 50% of malignancies, either alone or in combination with other chemotherapeutic treatments [3]. However, despite the advent of platinum resistance and the severe

side effects connected with chemotherapeutic therapies, new anti-cancer medications are still actively being looked after [4]. Numerous organometallic compounds, or molecules with at least one metal-carbon link, have demonstrated their potential as highly effective anti-cancer therapy candidates over the past few decades [5-8]. Organometallic complexes have a wide range of structural and stereochemical properties [9], that allow the rational design of ligands, and have a variety of action mechanisms, including redox activity, ligand exchange, catalytic activity, and/or photoactivity [9-13]. Relatively few examples of hazardous rhenium organometallic compounds are available in the literature, compared to certain widely studied organometallic complexes such as those based on ruthenium [14]. However, many studies describing the potential of such compounds have lately been reported [15]. Rhenium (Re) organometallic compounds do have a number of inherent qualities that are helpful for the development of model anti-cancer medication candidates. Many Re organometallic complexes, for instance, provide good luminescent probes because of their long-lasting emission states, significant Stokes shifts, high quantum yields, and tunable emissions [16-17]. Recently, the in vitro anticancer potency of seven synthesized Rhenium(I) tricarbonyl aqua complexes were reported by Knopf et al. (2017) aside from a few exceptions, all synthesized complexes were observed to possess inhibitory concentrations (IC50) of less than 20 μM in Hela cells; and therefore, suggest their suitability against cancer cells. Three complexes were overall, observed to possess a comparable anticancer potency against cisplatin-resistant cells and wild-type cells [18]. Moreover, the in vitro assay purported that complex 13 induces cell death without generating intracellular reactive oxygen species or depolarization of the mitochondrial membrane potential. Also, a revised synthesis of Rhenium[I]-diselenother complex was reported by Collery et al. (2015) and it exhibited anti-cancer potency against MDA-MB231 cells in vitro. It was also found to induce a considerable reduction in the volume of the primitive breast tumors and pulmonary metastases without causing significant toxicity [19-20]. In the same vein, the tricarbonyl rhenium isonitrile polypyridyl (TRIP) complex of King et al. (2019) was tested against HeLa cells employing the MTT assay. Several derivatives of the synthesized complexes were equally tested, and the findings demonstrate that the derivative containing isonitrile moiety was observed to be inactive against HeLa cells due to a decreased strength of electron-donating groups. Overall, the results indicated that the electron density of the ligand had a considerable influence on the cytotoxicity and anticancer potency of the ligands [21]. The anticancer properties of rhenium and ruthenium complexes containing N-heterocyclic carbene (NHC) ligand incorporated with

indomethacin were prepared and tested against pancreatic cancer cell lines. The findings of this research demonstrated that the rhenium complexes stimulated cell cycle arrest at the G2/M phase by inhibiting the phosphorylation of Aurora-A kinase. Also, a preliminary investigation on the QSAR of these complexes showed that the anticancer potency was mainly associated with the lability of the ancillary ligand [22]. Furthermore, a novel water-soluble rhenium diseleno-ether was proposed to assess the uptake potential of Re and Se atoms into the nucleus of malignant cells. The distribution of these atoms in the main organ after oral administration was tested. The research showed that Re was well incorporated into the nucleus of malignant cells in the most sensitive cells MCF-7 obtained from human breast cancer without the efflux of Re whereas a significant efflux of Re from the nucleus was attained after wash-out in MCF-7 resistant cells (MCF-7 Mdr and MCF-7 R) and Hela cells [19]. Furthermore, the cellular distribution and mode of action of most rhenium complexes can be well understood by conventional and/or time-resolved emission microscopy (such as FLIMS). Additionally, all known cytotoxic Re organometallic compounds are based on the $Re(CO)_3$ core, which is chemically stable and simple to obtain, for example, from the 1- to 3-step syntheses of $[Re(CO)_3(H_2O)_3]$ $+/[ReBr_3(CO)_3]$ [23-25] $Re(CO)_5Cl/Re(CO)_5Br$ [26-27], or $Re_2(CO)_{10}$ [28]. The incorporated ligands can be made to include additional functional moieties, including biomolecule-targeting ones [29]. However, the ability to create "hot" analogs that can be used for radio-imaging as well as for therapy is the main characteristic of the Re organometallic complexes. Due to the similarities in the coordination chemistry of these group 7 congeners, 99mTc can frequently be utilized with the same set of ligands as the cold Re in addition to ^{186}Re and ^{188}Re isotopes [30-31]. As a result, a Re complex has the potential to be a multimodal molecule that functions as a radio-imaging and therapeutic agent as well as a luminous probe. Additionally, "hot" analogs can be utilized to conduct in-vivo pharmacokinetic and bio-distribution investigations, both of which are crucial for the development of novel medications.

Based on these enormous inherent properties of rhenium complexes, and the various inimical increasing cancer reports, this study presents, the synthesis, spectroscopic characterization, DFT, and experimental and in-silico anticancer activities of Rhenium-imidazole-based derivative: ((R)-1,2-dimethyl-1,2-dihydro imidazole (**Re-1**) and 2-methyl $1\lambda^2,3\lambda^2$-imidazole (**Re-2**) is investigated in detail. DFT investigations have been sought to gain insight into the electronic properties of the synthesized complexes; the Hirshfeld surface analysis, intra and intermolecular interactions,

frontier molecular orbitals, and adsorption wavelength were all investigated to this end. The TD-DFT/ ẁB97XD, M06x-D3, and Pbe0-D3 with the Gen basis set were used to generate theoretical UV-Vis absorption of the titled complexes, which were then compared to the outcomes of experiments. Additionally, calculations involving natural bond orbitals (NBOs) have been carried out and assessed. Theoretical and experimental FT-IR data of **Re-1** and **Re-2** have also been examined for their vibrational assignments. More so, in-silico studies were performed on the two complexes (**Re-1** and **Re-2**), to examine their activities as potential anti-cancer agents.

2.0 Experimental and Computational Methodology

For synthesis and characterization, Strem Chemicals Newburyport (USA) and Sigma Aldrich (South Africa) were used, and all reagents were analytically graded unless stated otherwise. No further purifications or modifications were made to the reagents and organic solvents used during these experiments. We conducted all of the experiments under aerobic conditions using deionized water and methanol.

2.1 Instruments and analysis

For infrared (IR) characterization, a PerkinElmer FT-IR Spectrometer Spectrum two, operating in the $4000 - 370$ cm^{-1} region, was used to record the spectra. The IR is connected to a computer and has a built-in temperature cell regulator, accurate to 0.3 °C. All the IR spectra of the synthesized complexes were recorded at room temperature. A PerkinElmer Lambda XLS+ Ultraviolet/Visible (UV/Vis) spectrometer was used to collect the UV/Vis data using a 1.000 ± 0.001 cm quartz cuvette cell. The Nuclear Magnetic Resonance (NMR) data were acquired from a Bruker MHz nuclear magnetic resonance spectrometer operating at 400.00 MHz for ^{1}H and ^{13}C at room temperature with deuterated chloroform (CDCl$_3$) as the solvent.

2.2 Synthesis of complexes

For the synthesis of the precursor *fac*-[Re(Acac)(CO)$_3$(H$_2$O)], *fac*-[NEt$_4$]$_2$[Re(CO)$_3$Br$_3$] (1.0 eq) is dissolved in 7 ml of deionized water. To the solution, AgNO$_3$ (3.0 eq) was added and stirred for 24 hours at room temperature. The acetylacetone (2.0 eq), was added to the filtrate, with 36 hours of stirring, to form the white to light yellow product. To a solution containing 1.0 eq of *fac*-[Re(Acac)(CO)$_3$(H$_2$O)] in methanol, the monodentate ligands (1,2-dimethyl imidazole for **Re-1,** 2-methyl imidazole for **Re-2** (1.0 eq.) was added, and the mixture was stirred for 6 hours at

room temperature, to form light yellow solutions. These solutions were left to crystallize and form the desired complexes.

2.3 *fac*-[Re(Acac)(CO)$_3$(1,2-DiCH$_3$Im)] (Re-1)

White to yellow solid, yield 89%, IR (solid, vCO cm^{-1}): 2010, 1910, 1868. UV–Vis (nm): H$_2$O = 281.0; CH$_3$OH = 258; C$_2$H$_5$OH = 279; CHCl$_3$ = 282. ^{1}H NMR (400 MHz, chloroform-d_3) (ppm): δ 6.75 (dt, J = 11.0, 1.6 Hz, 2H), 5.33 (d, J = 1.2 Hz, 1H), 3.64 –3.55 (m, 3H), 2.62 – 2.54 (m, 3H), 1.94 – 1.88 (m, 6H). ^{13}C NMR (101 MHz, chloroform-d_3) (ppm): δ 147.69, 127.50, 120.49, 101.79, 33.80, 27.49, 12.75, Re-^{13}CO = 198.38, 187.73.

2.4 *fac*-[Re(Acac)(CO)$_3$(2-CH$_3$Im)] (Re-2)

White to yellow solid, yield 86%, IR (solid, vCO cm^{-1}): 2010, 1875. UV–Vis (nm): H$_2$O = 281.0; CH$_3$OH = 279; C$_2$H$_5$OH = 282; CHCl$_3$ = 281. ^{1}H NMR (400 MHz, chloroform-d_3) (ppm): δ 6.75 (d, J = 7.9 Hz, 2H), 5.32 (s, 1H), 3.59 (s, 3H), 2.57 (s, 3H), 1.91 (s, 6H). ^{13}C NMR (101 MHz, chloroform-d_3) (ppm): δ 127.47, 115.30, 100.96, 25.84, Re-^{13}CO = 197.32, 187.69.

2.5 Crystallography

Single crystals of selected **Re-1** and **Re-2** complexes were analyzed on a Rigaku XtaLAB Synergy R diffractometer, with a rotating-anode X-ray source and a HyPix CCD detector. Data reduction and absorption were carried out using the CrysAlisPro (version 1.171.40.23a) software package [32]. All X-ray diffraction measurements were performed at 150(2) K, using an Oxford Cryogenics Cryostat. All structures were solved by direct methods with SHELXTS-2013 [33] and refined using the SHELXL-2013 [33] algorithm. All H atoms were placed in geometrically idealized positions and constrained to ride on their parent atoms. For data collection and refinement parameters, see the SI (Tables SI1, SI2). The X-ray crystallographic coordinates for all structures have been deposited at the Cambridge Crystallographic Data Centre (CCDC), with deposition numbers CSD 2194486 and 2194485. The data can be obtained free of charge from The Cambridge Crystallographic Data Centre *via* www.ccdc.cam.ac.uk/data_request/cif.

2.6 Computational details

In other to ensure the stability of the structure and sensitivity to computational methods, optimization of the complexes was performed in both gas and solvent media by employing the Kohn-Sham density functional theory approach for multiple quantum mechanical computations. Using GaussView 6.0.16 [78] and Gaussian 16 [79], the studied structures were optimized using three

inclusive dispersions corrected functional ώB97XD, m06x-D3, Pbe0-D3 with the Gen basis set [34-37]. The ώB97XD, M062X-D3, and PBE0-D3 functional were used because they possess dispersion and long-range correlations, and thus can capture and report detail interactions which makes them more accurate than other functional. Frequency calculations were also performed at the same level of theory in other to ensure that the respective optimized structures correlate to the true energetic minima which are affirmed by the absence of imaginary frequencies, hence validating the absolute agreement of the optimized geometry to its respective energetic minima on the potential energy surface. Natural bond orbital (NBO) calculation was carried out using NBO 3.1 software [80] embedded in the Gaussian program. Origin, Visual Molecular dynamics (VMD), Crystal Explorer, and Avogadro software as well as multiwfn 3.7 dev [38-40] were employed to conduct Density of State (DOS), Hirshfeld Analysis, and Frontier molecular orbital visualizations respectively.

2.7   Molecular docking procedures

The selected proteins used for docking were downloaded from the protein data bank and prepared using Biova discovery studio software [81]. Before the preparation process of the selected protein, several breast cancer proteins (1g50, 1oqa, 1xyt, 2lwl, 2y6w, 3hb4, and 5w9d) were downloaded to carefully screened, and choose the best protein based on binding affinity, hydrogen bonding, Van der Waals interaction. The downloaded proteins were prepared by first defining the active or reactive sites in line with the visualized active pocket based on the interaction of the protein with the co-crystalized ligand as complexed in the protein data bank; then, removing water molecules as well as native ligands, that are not necessary during docking experiments and finally adding explicit hydrogen. The protein cavity was defined with X, Y, and Z coordinates of -34.265013, 10.400253, -13.145097 for 2y6w and 16.858512, 24.365038, and -14.537123 for 5W9d receptor with the size of 20Å respectively, after which the receptors format were converted to pdbqt using Auto dock 4.2 [82]. The preparation of the ligand was conducted by carrying out energy minimization at the DFT/ M062x-D functional with Gen basis set. About 11 receptors were docked with the investigated **Re-1** and **Re-2** complexes using Autodock vina and the resulting output was further visualized using BIOVA discovery studio and PyMol. The autoDock tool's default search algorithm and force field which works via the Lamarckian Genetic Algorithm (LGA) was employed throughout docking experiments. However, it was observed that the grading function in autoDock is primarily based on the number of hydrogen bonding, electrostatic interaction, Van der Waals interaction, entropy change on the binding of the studied complex to the protein as well as

solvation. Along the X, Y, and Z coordinates axes, the grid parameter file (GPF) was set 20×20×20Å, 20×20×20, and 20×20×20 respectively.

3.0 Results and Discussion:

3.1 Chemistry

fac-[Re(Acac)(CO)$_3$(1,2-DiCH$_3$Im)] (**Re-1**) and *fac*-[Re(Acac)(CO)$_3$(2-CH$_3$Im)] (**Re-2**), were prepared according to previously reported procedures, using a '2+1' approach [41-45]. The ^{1}H and ^{13}C NMR spectra of the Rhenium complexes reveal pure diamagnetic compounds owing to their facial arrangement and low spin *d*6 of the Re(I) metal ion (Figure. SI1a-SI2b). The carbonyl stretching bands are shown in the IR data (Figure. SI3, SI4) of complexes **Re-1** and **Re-2**, in the water-free region of the IR spectrum, as predicted for **Re-1** tricarbonyl complexes. All compounds exhibit very similar patterns of stretching IR vibrational frequency and intensity, with both symmetric and asymmetric CO stretching vibrations ranging between 2010 and 1868 cm^{-1}, respectively. The UV– Vis spectra (Figures SI5, SI6) of the complexes **Re-1** and **Re-2** in different solvents, display a metal-to-ligand charge transfer (MLCT) at an absorbance ranging between 258 and 282 nm, which is typical for rhenium tricarbonyl complexes bearing β-diketone ligands [42, 44, 46-47]. The spectroscopic values are summarized in Table 1. The solid-state X-ray crystal structures of complexes **Re-1** and **Re-2** are discussed in the next section.

Table 1: Spectroscopic values of rhenium tricarbonyl complexes.

Complex	IR CO Stretching (cm^{-1})	λ_{max} (nm)			
		H$_2$O	Methanol	Ethanol	Chloroform
Re-1	2010,1910,1868	281	258	279	282
Re-2	2010,1875	281	279	282	281

3.2 X-ray crystallography

Single crystals of **Re-1** and **Re-2** suitable for X-ray diffraction were obtained from their respective saturated methanol solutions. The molecular structures of **Re-1** and **Re-2** are shown in Figure 1. Corresponding tables containing crystallographic data and selected bond lengths and angles are included in the supplementary information (Tables SI1, and SI2). **The Re-1** complex was

crystallized in the monoclinic $P2_1/c$ with one molecule in the asymmetric unit, whereas the **Re-2** complex was crystallized in the triclinic $P\text{-}1$ space group with two crystallographically independent molecules in the asymmetric unit. Each Rhenium center exhibits a slightly distorted octahedral coordination sphere that is made up of three facially coordinated carbonyl ligands, one acetyl acetonato ligand, as well as one imidazolyl-based ligand. The deviation from an ideal octahedral geometry is indicated by the bond angles C_6-Re_1-C_7 (89.14(16) ° (**Re-1**), 86.1(3) ° (**Re-2**)), C_8-Re_1-C_6 (88.67(17) ° (**Re-1**), 87.3(3) ° (**2**)), O_1-Re_1-C_8 (93.03(14) ° (**Re-1**), 95.4(2) ° (**Re-2**)), as well as N_1-Re_1-$C6$ (96.26(14) ° (**Re-1**), 95.3(2) ° (**Re-2**)). The bidentate acetylacetonato ligand forms strong bonds to the Re center as signified by the average Re_1-O_{ave} bond lengths of 2.128(3) Å (**Re-1**) and 2.137(4) Å (**Re-2**), and O_1-Re_1-O_2 bite angles of 85.67(10) ° (**Re-1**) and 85.34(16) ° (**Re-2**), respectively. The coordination of the imidazole-based ligand in each case seemed to have a minimal effect on the bonding of the axial carbonyl ligand (C_8-O_5) *trans* to the imidazolyl ligand, as comparable equatorial (Re_1-C_{eq} = 1.909(5) Å (**Re-1**), 1.896(7) Å (**Re-2**)) and axial ($Re1$-$C8$ = 1.908(4) Å (**Re-1**), 1.925(8) Å (**Re-2**)) Re-C_{CO} bond lengths were observed. The substitution of the N-methyl group for the N-H group in the imidazolyl ligand for **Re-2** only slightly elongates the Re-C_8 bond (carbonyl ligand *trans* to Im-based ligand) due to the *trans* effect, as compared to the same bond in **Re-1**. This leads to a strengthening of the C-O bond (more triple bond character) with a concomitant shortening of the C_8-O_5 bond (1.143(9) Å for **Re-2** *compared to* 1.167(5) Å for **Re-1**). The Re_1-N_1 and Re_1-O_{ave} bonds are all comparable (2.197(3), 2.128(3) for **Re-1**, 2.211(5), and 2.137(4) for Re-2, respectively), and correlate with literature values [48-51]. The molecules of **Re-1** and **Re-2** pack in layers, in a back-to-front manner, as seen in the ac and bc planes (Figures SI5 and SI6 in the supporting information). These layers are stabilized by weak intermolecular C-H…O interactions. While there are no hydrogen bonds observed **Re-1** system, clusters of four molecules are grouped by four strong N-H…O hydrogen bonds (*c.a.* N-H…O = 172.89° and 155.64°, N-H = 0.88 Å, H…O = 2.00 Å and 2.18 Å for **Re-2**, see Figure SI6 in the supporting information).
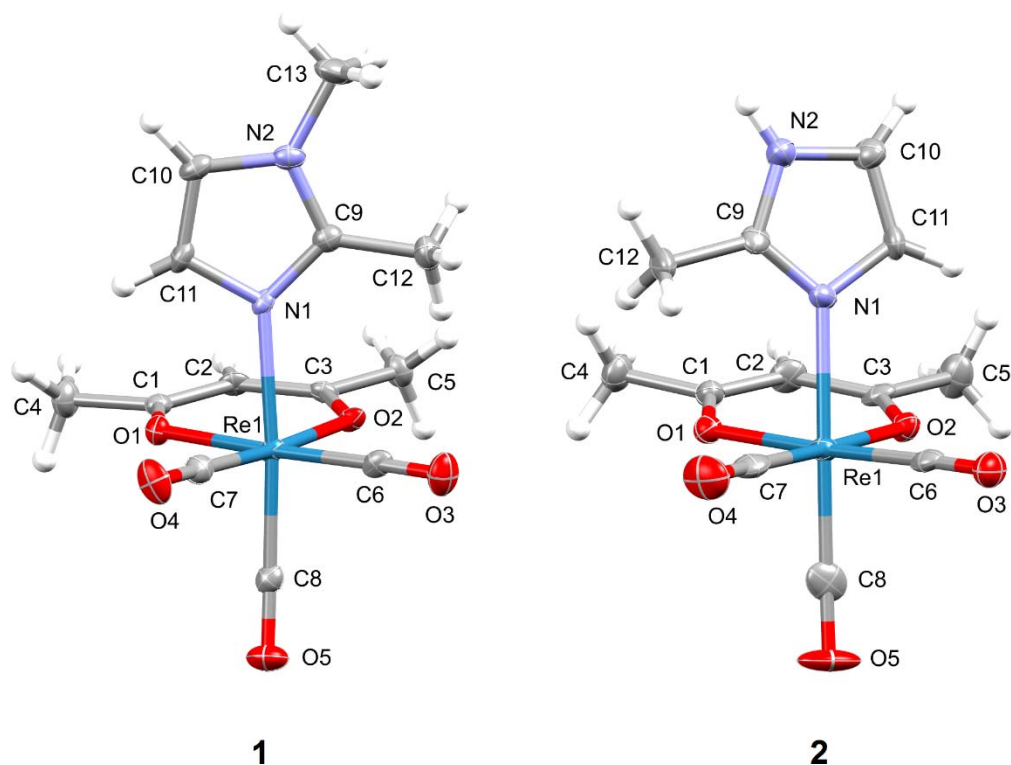
Figure 1. Molecular structures of **Re-1** and **Re-2**. Thermal ellipsoids are plotted at a 50% probability level.

3.3 Geometry optimization

In an attempt to ensure the sensitivity and stability of the optimized structure to computational methods, geometry optimization was executed in the gas phase using different functional ωB97XD, M06x-D3, and Pbe0-D3 with Gen basis set to check which functional best predicts the bond length and bond angles in tandem with their experimental counterparts for (R)-1,2-dimethyl-1,2-dihydro imidazole or **Re-1** and 2-methyl $1\lambda^2,3\lambda^2$-imidazole or **Re-2** optimized structures. it is important to ensure that the optimized structure is in correlation with the exact energetic minima, thus for this purpose, frequency optimization was carried out. The absence of imaginary frequency confirms that the given optimized structure correlates with the energetic minima, thus confirming the absolute agreement of the optimized geometry to its energetic minima on the potential energy surface. From the energetic parameters obtained, the optimized structures are said to be very stable. Table SI3 below shows the calculated geometry parameters of **Re-1** and **Re-2** in the gas phase. The calculated C-C bond C-N bond lengths were observed to fall within the range of 1.5236Å to 1.2757Å for both structures using different functionals. Also, for the C-O functional group, the

bond length was observed to deviate slightly from the experimental values with a difference of 0.0036Å – 0.1072Å respectively as clearly shown in Table SI3. The Root Mean Square Deviation (RMSD) from the obtained experimental data for bond length was 0.074682 Å, 0.044722 Å, and 0.045741 Å for (R) d, d imidazole, and 0.064822 Å, 0.08648 Å and 0.11965354 Å for 2-M1λ^2,3λ^2 imidazole structures. It was further observed that the RMSD for the M062x-D3 functional was very close to that of the experimental counterpart for (R) d, d imidazole optimized structures since the level of deviation from experimental data when the comparison is made with other functional is trifling or slightly negligible. More so, the C-C bond angle of (R) d, d imidazole was observed theoretically to be within the range of 107.2014º – 178.5623º and 105.300º - 179.015º from the experimental (XRD) values. However, a slight deviation was observed between the theoretical and experiment values in the range of 1.9014º - 0.4527º for both optimized structures. A similar trend was also observed for both C-O and N-C functional groups. In conclusion, the observed bond length and bond angles from Table SI3 revealed that the M062X-D3 functional best replicated the experimental values. Nonetheless, the computed values were all observed to be in close agreement with their experimental counterpart as clearly shown in Table 1 below.

3.4 Vibrational analysis

Fourier transform infrared is a resourceful tool for molecular characterization with applications in the pharmaceutical, plastics, and polymer industries as well as investigations of fundamental vibration using FT-IR vibrational analysis [52]. The vibrational properties of (R)-1,2-dimethyl-1,2-dihydro imidazole (**Re-1**) and 2-methyl 1λ^2,3λ^2-imidazole (**Re-2**) were theoretically computed to compare with the experimental FT-IR absorptions to properly estimate the absorptivity of the isolated compounds in the gas phase. The titled molecules were observed to exhibit 15 modes of vibration, 223 electrons with 37 atoms for complex 1 and 33 atoms, and 214 electrons with over 15 vibrational modes which are the same for both isolated compounds due to high similarity in their respective structures. Thus a detail elucidated comparison of the experimental FT-IR and theoretical results as well as the potential energy distribution (PED) assignments for the investigated compounds are carefully presented in Table 2. However, the isolated complexes were optimized by employing Density Functional Theory (DFT) method at M062X-D3 basis set using Gaussian16 and Gaussview 6.0.16 software while the spectrum was plotted using origin software.

3.4.1 CH, CC vibration

In the compounds under consideration, the weak absorption peak at 3122 cm^{-1} is assigned to the CH stretching vibration depicted in the experimental IR spectrum, while the calculated vibrations were observed to occur at 3239 cm^{-1} with potential energy distribution (PED) contribution of roughly 97.20%. However, it was observed that the peak at 3175cm^{-1} corresponds to CH asymmetric stretching vibration while CH bending deformation was observed to occur at 3150cm^{-1}, 3123 cm^{-1}, 3075 cm$^{-1,}$ and 1486 cm^{-1}. Interestingly slight drift in the absorption peaks was observed to occur between 3122 cm^{-1} and 3123 cm^{-1} wave numbers with a little difference of 1 cm^{-1} respectively. This slight difference observed between the experimental and calculated frequencies is due to slight differences in the structural orientation of the studied compounds. The calculated peaks at 1599 cm^{-1} and 1574 cm^{-1} are assigned to two different vibrational modes i.e aromatic C=C symmetric stretching as well as CH rocking bending deformation. Thus, the theoretical frequencies are in close correlation with the experimental FT-IR counterpart.
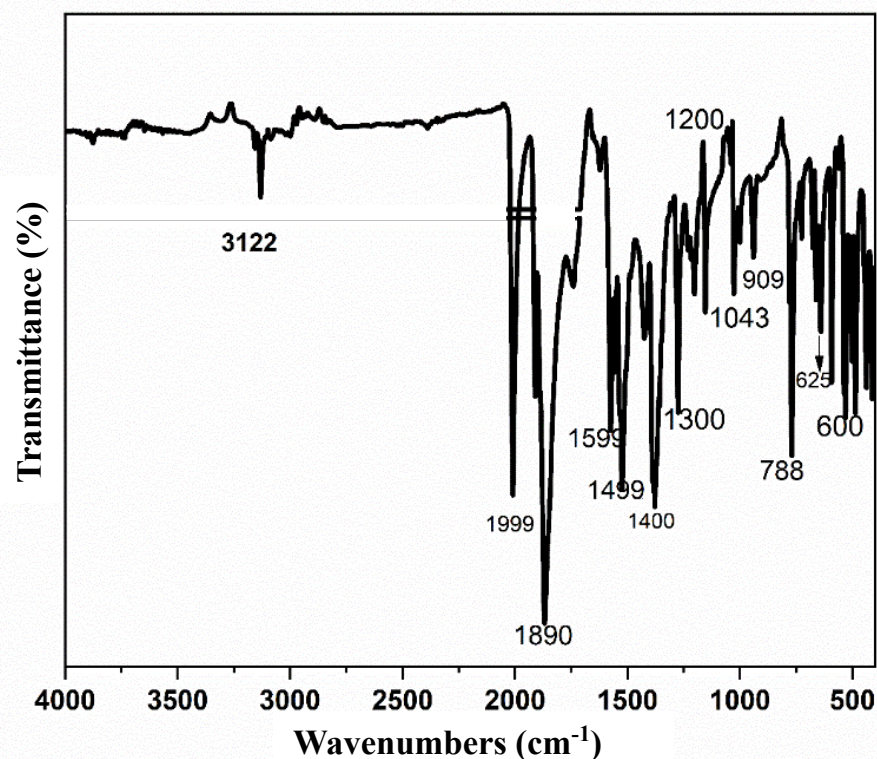

Figure 2. Experimental FTIR spectra for Rhenium tricarboxylic complexes

Table 2. Vibrational analysis calculated at DFT/M062X-D3/gen/LanL2DZ/def2svp

Mode	Expt	Calculated (Gas)	Relative intensity	Assignment
1	3122	3239	4.942	VssyCH(97.20)
2	3122	3175	6.246	VassyCH(96.5)
3	3122	3150	10.713	CH Twisting(97.04)
4	3122	3123	12.318	CH Rocking(97.03)
5	3122	3075	4.868	CH Twisting(97.02)
6	1999	2167	985.619	Vssy CO(79.86)
7	1999	2051	1292	Vassy CO(79.84)
8	1890	1681	643.72	CO Torsion deformation due to angle strain(76.17)
9	1599	1574	216.72	Vssy C=C, CH Rocking deformation,(98.19)
10	1599	1570	37.64	CH(98.05) Wagging deformation, Vssy C=N (98.15)
11	1499	1486	46.39	CH Twisting deformation(80.37)
12	1400	1418	11.50	Vssy C=N(86.35)
13	1300			CH Rocking deformation(92.46)
14	1200	1238	25.40	CH Rocking deformation(85.32)
15	1043	1044.81	14.34	CH Rocking deformation(96.88)

3.4.2 CO, CN vibration

The high absorption peak from the IR spectra studies as shown in Figure 2 corresponds to 1890 cm^{-1} and 1599 cm^{-1} wave numbers which are assigned to C=O and C≡ N functional groups.

However, the carbonyl functional group was observed to exhibit torsion bending deformation due to angle strain whereas the cyanide functional group exhibited symmetric stretching vibrational motion. Similarly, the theoretically calculated vibrations for the carbonyl functional group were observed to occur at 1681cm^{-1} from the IR spectra analysis meanwhile the calculated vibrational motion occur at 1570cm^{-1} with a corresponding PED contribution of roughly 76.17% and 98.15%.

3.5 Electronic Properties

3.5.1 Global quantum reactivity trend

The frontier molecular orbital (FMO) analysis is utilized for the qualitative assessment of molecular excitation capacities and electron transportation vehicles of the synthesized compounds. As such, the highest occupied molecular orbital (HOMO) and the lowest unoccupied molecular orbital (LUMO) of the synthesized studied Rhenium-Imidazole derivatives (**Re-1** and **Re-2**) are displayed in Figure 3. The FMO HOMO and LUMO representation are key parametric electronic quantifiers that, play a significant role in expounding the chemical stability of the studied compounds [53]. The highest occupied molecular orbital (HOMO) depicts the electrons-donating ability, whereas the LUMO denotes the electron-accepting capacity [54]. Per se, the molecular chemical reactivity was enunciated via the HOMO and LUMO energy gap, in addition to this justification, it is worthy to note that small energy gap values indicate higher chemical reactivity and less chemical stability. As conveyed, it is also pertinent to know that, the low HOMO-LUMO energy gap evolving in quantum reactivity represents the effective electronic charge transfer from HOMO to LUMO, which makes investigated compounds of interest more polarizable and vastly active. Accordingly, molecules partaking higher energy gap led to higher stability with lesser reactivity than its conjugate with a smaller energy gap [55].

To have a coherent understanding of the chemical reactivity and stability of the Imidazole derivative compounds (**Re-1** and **Re-2**), the parametric global chemical quantum descriptors like HOMO (E_{HOMO}), LUMO (E_{LUMO}), Energy gap (ΔE), ionization potential energy (I.P), Electron affinity (A), global chemical hardness (η), global chemical softness (S), Electronegativity index (χ), Electronic chemical potential (μ), and global chemical electrophilicity index (ω) were scrutinized, as tabulated in the preceding Table 3. Correlatively, the HOMO-LUMO energy difference also permits ascertaining the chemical reactivity, kinetic stability, chemical hardness, and softness of the synthesized compounds under investigation [56]. The identified molecules

exhibiting a lower energy gap are priory associated with the easy transference of electrons from the HOMO sites to the LUMO sites resulting in a greater chemical reactivity potency and affording good electronic activity than those with higher energy gaps [57]. With reference to this assertion, studied compound B (B~Re-Im2) exhibited a lower energy gap (ΔE) of 7.1570eV. As such, based on Koopman's theorem, the ionization energy and the electron affinity parameter for this study were calculated according to the following approximations [58-59].

$$I.P = -E_{HOMO}$$

$$A = -E_{HOMO}$$

More so, global chemical hardness (η) and chemical softness (S) are crucial calculations that have inferences on the stability of the molecular geometries of the compounds under study. Thus, the chemical hardness and global softness may be related to the energy gap between the HOMO and LUMO orbitals in a distinctive way that, the higher HOMO-LUMO energy gaps of the molecular systems of study tally with a more stable and very less reactive character. On the other hand, molecules with smaller HOMO-LUMO energy gaps designate highly reactive and less stable characters [60]. Hence, the chemical hardness and chemical softness of the titled compounds were calculated using the following formulae;

Chemical hardness (η)$=\frac{1}{2}(E_{LUMO} - E_{HOMO}) \equiv \frac{1}{2}(I.P - A)$

Chemical softness (S)$= \frac{1}{2\eta} \equiv \frac{1}{(I.P-A)} \equiv \frac{1}{(E_{LUMO}-E_{HOMO})}$

Consequently, the electronegativity index (χ) in relation to this study, measures the propensity of an atom to gain a bonding pair of electrons. Molecular electronic chemical potential (μ) and the global electrophilicity index (ω) were established by Paar and Pearson and the theoretically calculated formulae are given as;

Electronegativity (χ)$=\frac{I.P+A}{2}$

Molecular electronic chemical potential (μ)$=-\frac{1}{2}(I.P + A) \equiv \frac{1}{2}(E_{HOMO} - E_{LUMO})$

Electrophilicity index (ω)$=\frac{\mu^2}{2\eta}$

As such, from the illustrated Table 3 the compounds **Re-1** and **Re-2** exhibit higher ionization potential energies of 7.861eV and 8.089eV respectively, and lower electron affinity energy values of 0.534eV and 0.932eV. More so, the studied compounds **Re-1** and **Re-2** exhibit lower chemical hardness and higher chemical softness values, which indicates that these studied imidazole derivatives (**Re-1** and **Re-2**) are very chemically reactive with less stability, with preference to compound B (**Re-2**), exhibiting more reactivity compared to compound A (**Re-1**). The electronic chemical potential (μ) reveals the electronic charge transfer that occurs within the molecules in the electronic ground state and thus, describes the capability of electrons to be released from the equilibrium state. Whereas, the electrophilicity index explains the measurement of the change in energies with electron flow from the HOMO to LUMO regions. Hence, from the depicted Table 3 it can be noted that compound B (**Re-2**) has a higher negative value of chemical electronic potential and a higher flow rate of electrons within its molecules compared to the other studied imidazole derivative **Re-1.** Correspondingly, from the analyzed quantum descriptive parametric results [61], it could be deduced that the synthesized compounds of interest have good and distinctive global reactivity profiles, especially Compound B (**Re-2**), which consist of a lower energy gap and outstanding chemical reactivity key parameters
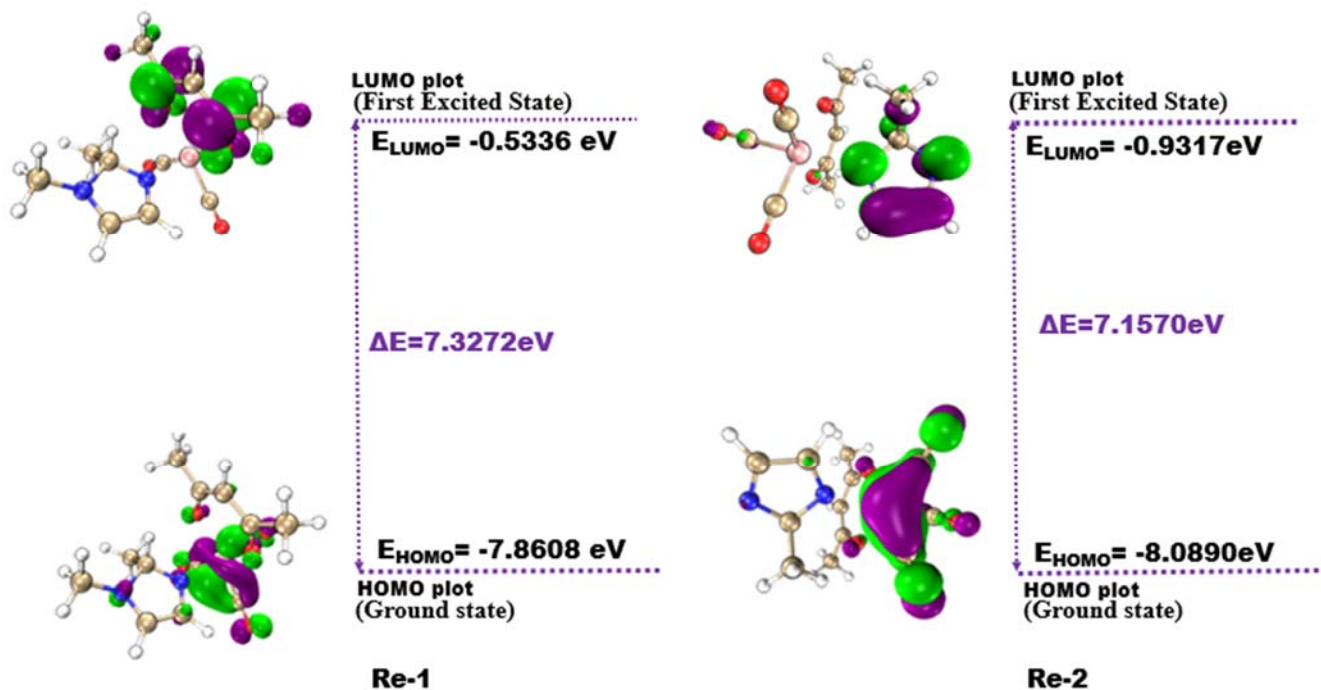

Figure 3: FMO iso-surface mapping of the studied complexes.

Table 3: Calculated key parameters of FMO energies and chemical quantum reactivity parameters of the studied imidazole derivatives calculated at DFT/M062X-D3/gen/LanL2DZ/def2svp.

Complexes	HOMO	LUMO	ΔE	I.P	A	χ	μ	η	S	ω
Re-1	-7.8608	-0.5336	7.3272	7.861	0.534	3.664	-3.664	4.197	0.239	1.599
Re-2	-8.0890	-0.9317	7.1570	8.089	0.932	4.510	-4.510	3.579	0.279	2.842

All calculated energy values are in electron volts (eV)

3.6 Stabilization energy analysis

Natural bond orbital (NBO) analysis sought to investigate the details of the intra-molecular, inter-molecular orbital bonding, conjugative interaction, hyper-conjugative interaction, and stabilization energies of compounds [62]. For this study, the natural bond orbital analysis was executed using the NBO 3.1 module entrenched in Gaussian 09 W package at DFT/ωB97XD theoretical density functional method with Gen basis set. Correspondingly, the relational donor-acceptor stabilization energy, $E^{(2)}(i{\rightarrow}j)$ for each donor (i) NBO and acceptor (j) NBO is given by the formula:

$$E^{(2)} = q_i \frac{(F_{i,j})^2}{\varepsilon_j - \varepsilon_i}$$

Where q_i is denoted as the orbital occupancy, i, and j are the Fock diagonal elements, and $F_{i,j}$, the off-diagonal NBO Fock matrix electronic element. Hence, the greater magnitude of conjugation enjoyed by the studied molecular system is a result of the enormous values of their stabilization energy ($E^{(2)}$), expressed in energy units of kcal/mol. As such, the most interacting donor NBO, acceptor NBO, and the large value stabilization energies of the studied imidazole derivative structures are keenly presented in Table 4. The utmost substantial donor-acceptor NBO interactions associated with the titled compounds were found to occur significantly between LP(1) $C_6 \rightarrow \pi^*O_2$-C_5 and LP(1) $C_6 \rightarrow \pi^*O_3$-C_4 natural bond orbitals having stabilization energies of 91.17 kcal/mol and 80.0 9kcal/mol for the **Re-1** compound and between LP(1) $C_6 \rightarrow \pi^*O_3$-C_4, LP(1) $C_6 \rightarrow \pi^*O_2$-C_5, σ^*Re_1-$N_{26} \rightarrow \sigma^*Re_1$-$O_3$, and $\sigma^* Re_1$-$N_{26} \rightarrow \sigma^*Re_1$-$O_2$ NBOs having corresponding stabilization energies of 205.87 kcal/mol, 200.41 kcal/mol, 95.94 kcal/mol, and 95.93 kcal/mol. Respectively for the **Re-2** compound. Thus, the highest stabilization energies for the studied compounds were observed to have occurred at the σ Re_1 - $O_{19} \rightarrow$ LP(1) C_{18} and LP(1) $C_6 \rightarrow \pi^*O_3$-C_4 donor-acceptor bonding orbitals in the **Re-1** and **Re-2** compounds, with noteworthy stabilization energies of 318.27 kcal/mol, 205.87 kcal/mol., and least perturbation energies of 62.95kcal/mol and 82.98

kcal/mol, occurring at the LP(2) $N_{26}\rightarrow$ LP*(1)Re$_1$ and LP(3)Re$_1\rightarrow \sigma$*Re$_1$-N$_{26}$ within the titled compounds [63].

Table 4: Second-order perturbation energy analysis of Fock matrix for the studied compounds calculated at DFT level of B97XD/Gen.

S/No	Donor NBO	Acceptor NBO	$E^{(2)}$/(kcal/mol.)	E(j)-E(i)/a.u	F(I,j)/a.u
			Re-1		
1	σ Re$_1$ - O$_{19}$	LP(1) C$_{18}$	318.27	0.16	0.293
2	LP(2) O$_{19}$	π*Re$_1$-C$_{18}$	99.17	0.39	0.250
3	LP(1) C$_6$	π *O$_2$-C$_5$	91.43	0.19	0.180
4	LP(1) C$_6$	π *O$_3$-C$_4$	80.09	0.20	0.175
5	LP(2) N$_{26}$	LP*(1)Re$_1$	62.95	0.78	0.289
			Re-2		
6	LP(1) C$_6$	π*O$_3$-C$_4$	205.87	0.16	0.175
7	LP(1) C$_6$	π*O$_2$-C$_5$	200.41	0.17	0.176
8	σ*Re$_1$-N$_{26}$	σ*Re$_1$-O$_3$	95.94	0.02	0.087
9	σ* Re$_1$-N$_{26}$	σ*Re$_1$-O$_2$	95.93	0.03	0.107
10	LP(3)Re$_1$	σ*Re$_1$-N$_{26}$	82.98	0.43	0.190

Consequently, it can be deduced from the analyzed NBO study that the particular spatial orientations of the investigated Imidazole-Rhenium derivatives arise from their respective stabilization energies, with relational orbital contribution occurring mostly in the **Re-2** compound, which is coherent with the other studied electronic properties.

3.7 Density of State (DOS)

The density of the state of a system (DOS) is an essential phenomenon in solid-state physics, as it elucidates the proportion of states that are to be occupied and the exact number of states corresponding to a unit energy interval [64]. However, due to the disparity in energy levels of isolated systems, the concept of DOS becomes questionable. Nevertheless, deliberations on the distinct quantum levels of curves have generated an essential tool (DOS graph) for representing and visualizing the individual contributions of molecular orbitals to various identified quantum states. Density of state can be used to elucidate the distribution of molecular orbital level of molecules, while the curves at the DOS plot designate the actual number of molecular orbitals at different quantum states in each respective energy interval [64]. To further comprehend the behavior of each fragment present in A~Re-Im1 and B~Re-Im2 compounds, the total density of state (TDOS) map, and partial DOS (PDOS) map, with individual contributions from different molecular orbitals, were plotted using Multiwfn and Origin as elucidated in Figure 4 where the orbital properties are

conspicuously shown in different energy ranges. Hence it is observed that the hydrogen atom gave the highest contribution to the PDOS between -0.7 to -0.35 a.u while the oxygen atom gave the least contribution to the molecular orbital for the **Re-1** complex in the range of -0.6 a.u to -0.45 a.u. Furthermore, similar chemistry is exhibited by plot **b** as the hydrogen atom gave the least contribution to the highest occupied molecular orbital (HOMO) at the PDOS region between -0.6 a.u to -0.45 a.u. Interestingly both plots reveal that hydrogen molecular orbital also contributed more at the LUMO between -0.18 to -0.10 a.u and -0.23 to 0.10 a.u for both plots respectively [65]. Thus, there is a slight shift in the LUMO orbital of **b** compared to **a**, therefore **a** is considered more stable as shown in Figure 4. This slight decrease in LUMO orbital is responsible for the molecular stabilization of the **Re-1** complex which is in tandem with the electronic studies as the **Re-1** complex has the least total second-order perturbation energy $E^{(2)}$ of 651.91 kcal/mol with energy gap (ΔE) of 7.3273 eV while **Re-2** complex had the highest $E^{(2)}$ energy of 681.13 kcal/mol with ΔE of 7.1570 eV. Thus, the DOS plot gave a clearer pictorial representation of the contributions from molecular orbitals to the stability of the A~Re-Im1 complex which correlates with the electronic studies.
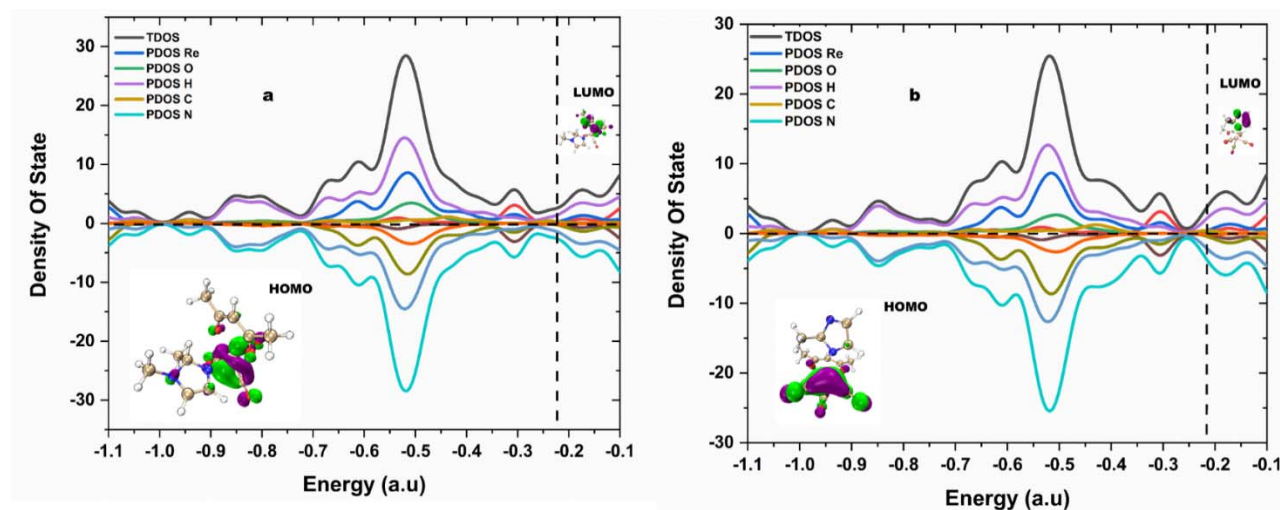

Figure 4: Density of state plots of the investigated Re-complexes; (a): **Re-1**, (b): **Re-2**, showing their different elementary fragment contributions.

3.8 Hirshfeld surface analysis

Hirshfeld surface (HS) analysis serves as a dominant tool for gaining additional intuition into the intermolecular interaction of molecular crystals, it allows a qualitative and quantitative

visualization and investigation of intermolecular close contacts in molecular crystals [66]. Hence, for this study, HS analysis iso-surface plots and the corresponding fingerprint plots (FPs) were utilized in analyzing the contribution and percentage of distinct intermolecular interactions to the crystal packing [67] of the titled compounds (**Re-1**, **Re-2**). Hence, the directions and strengths of intermolecular interactions within the molecular crystals are priories mapped onto Hirshfeld surfaces defined by the descriptor (d_{norm}), which is given in equation X, where r_i^{vdw} and r_e^{vdw} are the respective van der Waals radii of the apposite atoms internal and external to the surface of the studied structures [68]. To distinguish the interatomic contacts within the studied compounds, a red, white, and the blue color map is used, which topologically represents the HS calculated from the d_{norm}. As the normalized contact distance (d_{norm}) is fundamentally based on both contact distance between the nearest atoms present inside (d_i) the investigated systems and outside (d_e) of the surfaces, representatively. Per the color maps on the surface of the studied systems, the red spot depicts the shortest intermolecular contacts and stronger interactions whereas, the white and blue spots represent medium interaction; the distance of contacts is exactly equal to the van der Waals separation with absolute d_{norm} value of zero and weaker interaction; longer contacts with positive d_{norm} value, respectively [69].

$$d_{norm} = \left(\frac{d_i - r_i^{vdw}}{r_i^{vdw}}\right) + \left(\frac{d_e - r_e^{vdw}}{r_e^{vdw}}\right)$$

As plotted, Figure 5 indicates the significant visible interactions on the HSs as well as in the 2D fingerprints illustrated. Re⋯H/H⋯Re, H⋯H, C⋯H/H⋯C, N⋯H/H⋯N, and O⋯H/H⋯O intermolecular interactions exist in the plotted fingerprints of **Re-1**. With specific percentage values of 0%, 28.5%, 19.2%, 3.2%, and 43.1%. Hence, with O⋯H/H⋯O interactions exhibiting the largest share in the crystal packing of **Re-1**, with a Hs percentage value of 43%. Whereas, the Re⋯H/H⋯Re with a percentage HS contribution of 0.0% has the smallest hydrogen bond interaction share in the aforementioned compound. Consequently, the analyzed intermolecular interactions within the **Re-2** compound were observed to occur with HSs percentage contribution of 0%, 39.6%, 2.1%, 13.5%, 31.9% for Re⋯H/H⋯Re, O⋯H/H⋯O, N⋯H/H⋯N, C⋯H/H⋯C, H⋯H interactions, with corresponding higher contribution from the O⋯H/H⋯O interaction and less bonding interaction accompanied with Re⋯H/H⋯Re bond, with respective HSs percentage contribution of 39.6% and 0%, respectively [70]. Accordingly, the respective contact analysis for the studied compound suggests that O⋯H/H⋯O hydrogen bonds are the driving force in the molecular

arrangement and crystal packing formation of the titled compounds. As such, the full interactions and the respective intermolecular interactions with their HSs percentages of the studied imidazole derivatives are shown in Figure 5. Therefore, it is noteworthy that the HS and their 2D-fingerprint plots are very distinctive tools for getting information about the contributions of respective intermolecular inter-contact that provide the stabilization of the molecular structures of the studied compounds.
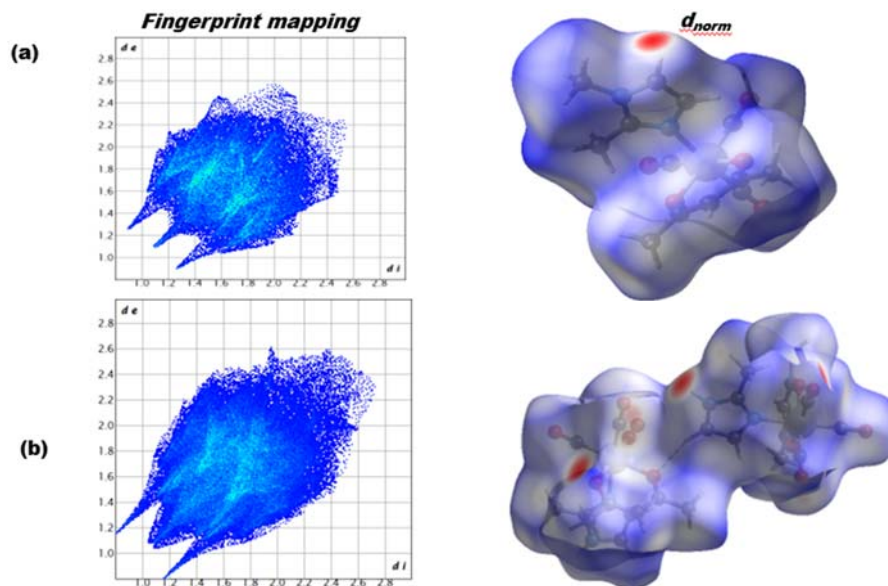

Figure 5: Two-dimensional fingerprint plots and Hirshfield surface mapping of the studied complexes; (a): **Re-1** and (b): **Re-2**.
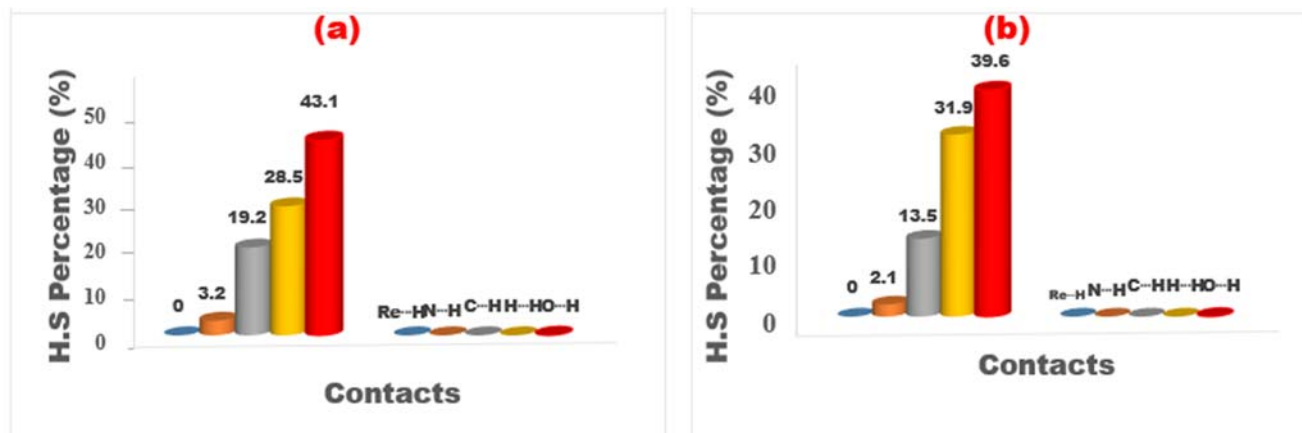

Figure 6: Analysed intermolecular interactions and their contributing percentages of the titled studied complexes; (a): **Re-1** and (b): **Re-2**, respectively.

3.9 UV-Vis spectroscopy

Quantum chemistry is essential in that it not only reliably predicts main absorption characteristics, it, however, unveils the possibility to fully comprehend all necessary information relating to optical spectra including; the direct correlation of optical properties with the fundamental chemical structure using MO description as well as higher-lying electronic transition and their strength of absorption [71]. The UV or visible spectrum of **Re-1** and **Re-2** enables us to carefully study molecules containing π electrons or non-bonding electrons (n-electrons) which are able to absorb ultraviolet-visible light energy and be excited into higher anti-bonding molecular orbitals. The amount of discrete wavelength of ultraviolet-visible light absorbed or transmitted through **Re-1** and **Re-2** compounds enable us to carefully study the influence of solvatochromic shift, bathochromic and hypsochromic effect on the studied complexes which are discussed in detail. From Table 5 the major transitions are HOMO-LUMO in all different solvents tested, as such minimal absorption with 18% and 2.318% molecular orbital contribution were observed from HOMO-2 to LUMO excitation for both complexes. Excitation in all solvents studied where basically from sigma to pi character σ→π* with Rhenium molecular orbital contributing chiefly to the σ→π* character due to the unavailability of lone pairs, as depicted by the atom's electronic configuration. It was observed that during the experimental process, no absorption in the visible region occurred, which implies the isolated compounds are colorless. However, the absorption maxima for **Re-1** and **Re-2** complexes were observed to fall within the range of 260 nm-363 nm, due to solvatochromism. From Table 5 A bathochromic shift was observed from water to chloroform with a difference of 13nm for **Re-1**. Similarly, **Re-2** was observed to exhibit a hypsochromic shift with a difference of 84nm. Theoretically, λmax for **Re-1** fall within the range 398.71nm to 399.53nm while the **Re-2** complex exhibit a kind of hypsochromic shift with λmax between 302.77nm-308.81nm, which is due to the difference in computational methods. Table 5 reveals that there is a relationship between the energy of excitation, oscillator strength, and percentage contribution of **Re-1** and **Re-2** complexes. Thus, as the energy of excitation increases from 3.01032ev to 3.1097ev, a corresponding increase in the percentage contribution was observed from 68.363%-75.989% for **Re-1** studied compound. However, the same trend was observed for the **Re-2** complex, as the solvent with the high energy of excitation has a corresponding high percentage value and oscillator strength.
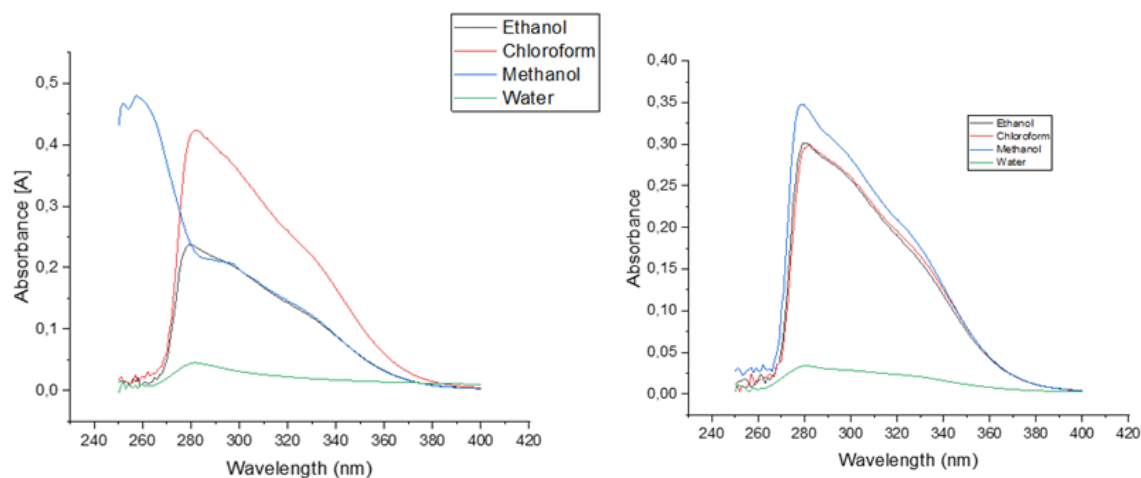
Figure 7: UV/Vis spectra of **Re-1** and **Re-2** in different solvents.

Table 5. Theoretical UV calculation in different solvent media calculated at DFT/M062X-D3/gen/LanL2DZ/def2svp

Systems	Excitation type	Experimental λmax	Theoretical λmax	Energy	Oscillator strength	% Contribution	Assignment
Re-1	Methanol **S0 → S1**	258	398.77	3.1091	0.0000	**H → L** 75.736%	$\sigma \to \pi *$
	Ethanol **S0 → S1**	279	398.81	3.1088	0.0000	**H → L** 75.590%	$\sigma \to \pi *$
	Chloroform **S0 → S1**	282	399.53	3.1032	0.0001	**H → L** 68.368%	$\sigma \to \pi *$
	Water **S0 → S1**	281	398.71	3.1097	0.0000	**H → L** 75.989%	$\sigma \to \pi *$
Re-2							
	Methanol **S0 → S1**	279	303.29	4.0880	0.0271	**H → L** 82.0557%	$\sigma \to \pi *$
	Ethanol **S0 → S1**	282	303.61	4.0837	0.0278	**H → L** 82.266	$\sigma \to \pi *$
	Chloroform **S0 → S1**	281	308.81	4.0149	0.0308	**H → L** 84.992	$\sigma \to \pi *$
	Water **S0 → S1**	281	302.77	4.0950	0.0270	**H → L** 81.685	$\sigma \to \pi *$

3.10   Molecular docking analysis

3.10.1 Criterial for protein selection

The estrogen receptors alpha [ERa] and beta [ErB] receptors were chosen due to their involvement as nuclear transcription factors responsible for the regulation of many complex physiological processes in humans. The inflection of these receptors by potential therapeutic agents is presently being considered for the preclusion and treatment of diverse pathological conditions, including cancer and cardiovascular diseases or inflammation [72]. The physiological functions of estrogenic compounds are moderated mostly by the estrogen receptors subtypes alpha [ERa] and beta. These proteins have actions in the cell nucleus, regulating the transcription of specific target genes by binding to associated DNA regulatory sequences [73]. The BRCA1 (10qa) is a tumor suppressor protein associated with breast and ovarian cancer. The C-terminal region of BRCA1 consists of two closely spaced BRCT domains that mediate essential biological functions, including regulation of transcription and control of cell-cycle progression by their interaction with phosphorylated effector proteins [74]. Moreover, the human β-defensins (hBDs) (2lw1) are perceived to act as alarm signaling molecules that stimulate the adaptive immune system in the presence of a threat. Defensin receptors also pose antimicrobial activity, as well as perform several other functions including chemoattraction of a variety of cell types to the sites of inflammation [75]. Oestradiol is a well-characterized sex hormone that stimulates breast cancer and other estrogen-related diseases. 17 beta-hydroxysteroid dehydrogenase type 1 (17beta-HSD1) catalyzes the last step in the synthesis of oestradiol and androstenediol in breast tumour tissue. The enzyme's high expression and activity after simultaneous blockade of estrogen receptors and inhibition of aromatase in the tumour show the necessity for its inhibition as a requirement for breast cancer therapy [76].

3.10.2 Discussion

The application of **Re-1** and **Re-2** ligands as an effective anti-breast cancer drug was examined using a docking experiment. The following proteins: 1g50, 1Oqa, 1xyt, 2w6w, 2lwl, 3hb4, and 5w9d were docked with **Re-1** and **Re-2** drugs to screen which protein best binds with the studied compounds effectively at the correct target sites. The results of these screenings are presented in the supporting information file Table SI4. However, 2y6w and 5w9d were observed to bind more effectively compared to other tested receptors and therefore were chosen for further studies [77]. The

results of the best conformation with the associated interacting amino acid residues, binding affinity, and interaction distances are carefully presented in Figure 8 and Table 6 from the obtained docking results, the experiment discloses a promising result, as such the valid form of interaction used to justify the binding affinities are only based on hydrogen bond formation. **Re-1** and **Re-2** compounds were observed to form a hydrogen bond with A: ARG95, GLY90, ARG95, and GLY89 amino acid residues of the 5W9d receptor as shown in Table 6 While hydrogen bond formation with THR347, ALA350, and UNK0 amino acid residues was observed from the visualized interactions with 2w6w protein/**Re-1** ligand, whereas the docking experiment reveals that **Re-2** complex formed a hydrogen bond with ARG95, GLY90, and UNK0 amino acid residues. It was further observed that there was hydrogen bond formation with ALA350 and UNK0 amino acid residues of the 2w6w receptor, as such, the proposed drugs bind favorably with the selected breast cancer receptors. However, the 2w6w receptor interacted with both complexes at a bond distance of 1.91, 2.35, 3.09Å, and 2.22, 2.02, 3.45, 2.79, 2.81Å respectively. The observed bond distance for the 5w9d receptor for both complexes docked are somewhat similar, thus the bond distance from Table 6 and Figure 8 suggests very good compatibility between the investigated ligands and the selected breast cancer receptors. The binding score obtained upon docking both ligands against the 2w6w receptor is -6.8kcal/mol and -6.9kcal/mol respectively. Interestingly when both ligands were docked against the 5w9d receptor, it appears that the **Re-1** drug bind more with a binding affinity of -6.7kcal/mol while the **Re-2** ligand was observed to have a binding score of -6.5kcal/mol. These suggest that both ligands have a high relative binding score but from our electronic studies, the **Re-1** drug is less stable and more reactive as explicated by the energy gap (E_g) of 7.3272ev while the **Re-2** compound was observed from Table 3 to have energy gap (E_g) of 7.1570ev and total second-order perturbation energy $E^{(2)}$ of 406.26, 191.87 and 82.98kcal/mol for LP→ π*, σ* → σ* and LP→σ* interaction respectively, which is comparably higher than $E^{(2)}$ for **Re-1** ligand from Table 3 and Table 4. **Re-2** ligands are observed to possess stronger hydrogen bonds than the **Re-1** complex, suggesting stronger and more excellent interactions. Comparing the binding affinity of the studied molecules with known inhibitors of the respective proteins shows a comparable binding affinity with the studied proteins. The redocked experiments with 5w9d protein show a binding affinity of -5.7 kcal/mol while the interaction of the co-crystalized ligand with 2y6w expressed a binding affinity of -9.0 kcal/mol. Both the studied compounds and the co-crystalline ligands were observed to bind similarly with the studied proteins. The RMSD for the

redocking experiments was calculated to be 0.376 and 1.641 for 5w9d and 2y6w respectively, therefore, confirming that the right active pocket was selected for interaction. In the same vein, similar amino acids were observed for the interactions of the known inhibitors of the selected proteins, these amino acids were: GLY, ARG, and ALA respectively. There are various literature claims asserting that the effectualness of a docking result is primarily graded concerning several hydrogen bonds, other binding configurations as well as stabilizing interactions like hydrophobic contact, pi-alkyl interaction, pi-sulfur interaction, and van der Waals interactions. Thus, our conclusion is based on this claim as obviously the docking experiments correlate with the obtained results from our previous studies reported.

Table 6. Docking score, receptor, and interacting amino acids during docking.

| 2w6w Receptor	Binding Affinity	Interacting amino acids	5w9d Receptors	Binding Affinity	Interacting amino acid residues
Re-1	-6.8	A:ARG95:HH22 - :UNK0:O 1.90861	**Re-1**	-6.7	A:THR347:HG1 - :UNK0:O 2.85651
		B:GLY90:HN - :UNK0:O 2.35223			A:ALA350:HN - :UNK0:O 3.07183
		B:ARG95:HE - :UNK0:O 3.09886			:UNK0:C - :UNK0:O 2.79562
		A:GLY89:CA - :UNK0:O 3.69379			:UNK0:C - :UNK0:O 2.80842
					:UNK0:C - :UNK0:O 2.74952
Re-2	-6.9	A:ARG95:HH12 - :UNK0:O 2.2219	**Re-2**	-6.5	A:THR347:HG1 - :UNK0:O 2.85494
		A:ARG95:HH22 - :UNK0:O 2.02047			A:ALA350:HN - :UNK0:O 3.07578
		B:GLY90:HN - :UNK0:O 3.45356			:UNK0:C - :UNK0:O 2.79335
		:UNK0:C - :UNK0:O 2.79337			:UNK0:C - :UNK0:O 2.80841
		:UNK0:C - :UNK0:O 2.80737			:UNK0:C - :UNK0:O 2.75597
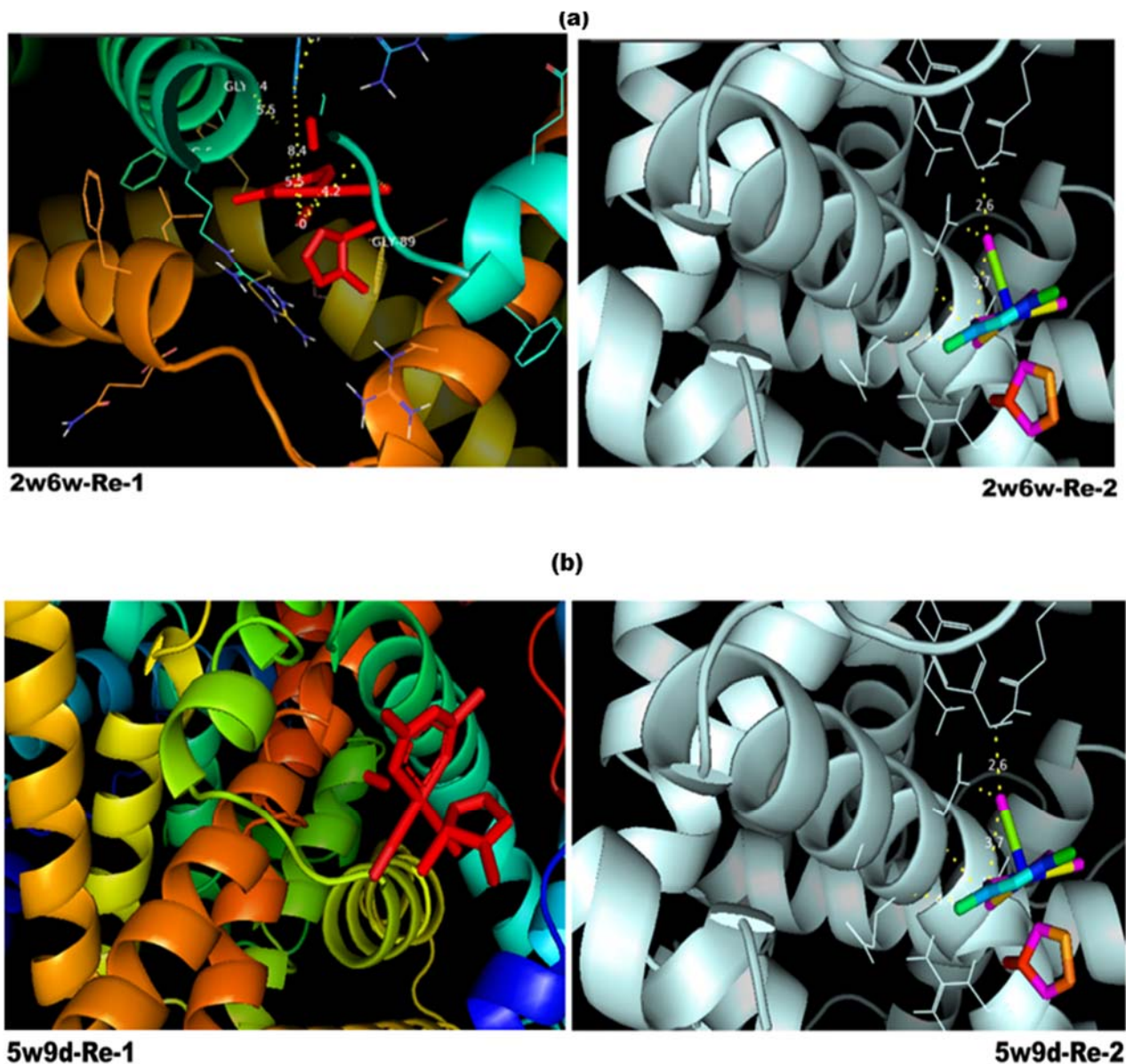
Figure 8: Docked conformers of the studied compounds with selected receptors.

4.0 Conclusions

The synthesis, X-ray characterization, and *in-silico* molecular docking investigation of formulated Rhenium complexes (**Re-1** and **Re-2**) are reported herein. The interaction of **Re-1** and **Re-2** ligands with 2w6w and 5w9d breast cancer receptors was investigated by utilizing high-level computational methods: PBE0-D3, M062X-D3, ẁB97XD. The isolated compounds were characterized using FT-IR as well as the NMR technique. Molecular properties like NBO and FMO were assessed to acquire insight into the molecular stabilization, charge delocalization as well as

reactivity of the investigated compounds. The experimental results divulged that the spectroscopic study is in tandem with the theoretical counterpart obtained using density functional theory. Also, the **Re-2** drug was observed to be stabilized by resonance delocalization between lone pair (LP) orbital to anti-bonding pi (π^*) orbital, and anti-bonding to antibonding sigma (σ^*) orbitals. The geometric study of **Re-2** shows excellent conformity with the experimental structure derived from x-ray crystallography. However, the root mean square deviation (RMSD) of experimental and computed bond lengths were observed to be 0.074682Å, 0.044722Å, and 0.045741Å for **Re-1**, meanwhile a slight difference was observed for **Re-2**. The m062x-D3 method replicated the experimental structural geometry of the synthesized complexes more accurately. Molecular docking revealed that **Re-2** possesses more excellent anti-cancer potency than **Re-1.** Thus, from our obtained results, the efficacy of **Re-2** to inhibit the growth of breast cancer cells is optimum.

5.0 Declarations

5.1 Acknowledgment:

5.2 Conflict of interest:

The authors declare no conflict of interest.

5.3 Funding

References

1.	Paprocka, R.; Wiese-Szadkowska, M.; Janciauskiene, S.; Kosmalski, T.; Kulik, M.; Helmin-Basa, A., Latest developments in metal complexes as anticancer agents. *Coordination Chemistry Reviews* **2022,** *452*, 214307.

2.	Yousuf, I.; Bashir, M.; Arjmand, F.; Tabassum, S., Advancement of metal compounds as therapeutic and diagnostic metallodrugs: Current frontiers and future perspectives. *Coordination Chemistry Reviews* **2021,** *445*, 214104.

3.   Irfandi, R.; Santi, S.; Raya, I.; Ahmad, A.; Ahmad, F.; Sari, D. R. T.; Prihantono, Study of new Zn(II)Prolinedithiocarbamate as a potential agent for breast cancer: Characterization and molecular docking. *Journal of Molecular Structure* **2022,** *1252*, 132101.

4.   De Castro, F.; De Luca, E.; Benedetti, M.; Fanizzi, F. P., Platinum compounds as potential antiviral agents. *Coordination Chemistry Reviews* **2022,** *451*, 214276.

5.   Pereira, S. A. P.; Baptista, L. A.; Biancalana, L.; Marchetti, F.; Dyson, P. J.; Saraiva, M., Automated approach for the evaluation of glutathione-S-transferase P1-1 inhibition by organometallic anticancer compounds. *J Enzyme Inhib Med Chem* **2022,** *37* (1), 1527-1536.

6.   Almeida, C. M.; S. Marcon, P. H.; Nascimento, É. C. M.; Martins, J. B. L.; Chagas, M. A. S.; Fujimori, M.; De Marchi, P. G. F.; França, E. L.; Honorio-França, A. C.; Gatto, C. C., Organometallic gold (III) and platinum (II) complexes with thiosemicarbazone: Structural behavior, anticancer activity, and molecular docking. *Applied Organometallic Chemistry* **2022,** *36* (8), e6761.

7.   Han, T.; Wu, Y.; Han, W.; Yan, K.; Zhao, J.; Sun, Y., Antitumor Effect of Organometallic Half-Sandwich Ru(II)–Arene Complexes Bearing a Glutathione S-Transferase Inhibitor. *Inorganic chemistry* **2021,** *60* (17), 13051-13061.

8.   Gupta, S.; Vandevord, J. M.; Loftus, L. M.; Toupin, N.; Al-Afyouni, M. H.; Rohrabaugh, T. N., Jr.; Turro, C.; Kodanko, J. J., Ru(II)-Based Acetylacetonate Complexes Induce Apoptosis Selectively in Cancer Cells. *Inorganic chemistry* **2021,** *60* (24), 18964-18974.

9.   Mohan, B.; Estalayo-Adrián, S.; Umadevi, D.; la Cour Poulsen, B.; Blasco, S.; McManus, G. J.; Gunnlaugsson, T.; Shanmugaraju, S., Design, Synthesis, and Anticancer Studies of a p-Cymene-Ru(II)-Curcumin Organometallic Conjugate Based on a Fluorescent 4-Amino-1,8-naphthalimide Tröger's Base Scaffold. *Inorganic chemistry* **2022,** *61* (30), 11592-11599.

10.   Muzzi, B.; Albino, M.; Gabbani, A.; Omelyanchik, A.; Kozenkova, E.; Petrecca, M.; Innocenti, C.; Balica, E.; Lavacchi, A.; Scavone, F.; Anceschi, C.; Petrucci, G.; Ibarra, A.; Laurenzana, A.; Pineider, F.; Rodionova, V.; Sangregorio, C., Star-Shaped Magnetic-Plasmonic Au@Fe3O4 Nano-Heterostructures for Photothermal Therapy. *ACS Applied Materials & Interfaces* **2022,** *14* (25), 29087-29098.

11.   Cervinka, J.; Gobbo, A.; Biancalana, L.; Markova, L.; Novohradsky, V.; Guelfi, M.; Zacchini, S.; Kasparkova, J.; Brabec, V.; Marchetti, F., Ruthenium(II)–Tris-pyrazolylmethane Complexes Inhibit Cancer Cell Growth by Disrupting Mitochondrial Calcium Homeostasis. *Journal of Medicinal Chemistry* **2022,** *65* (15), 10567-10587.

12.   Shen, W. Y.; Jia, C. P.; Liao, L. Y.; Chen, L. L.; Hou, C.; Liu, Y. H.; Liang, H.; Chen, Z. F., Copper(II) Complexes of Halogenated Quinoline Schiff Base Derivatives Enabled Cancer Therapy through Glutathione-Assisted Chemodynamic Therapy and Inhibition of Autophagy Flux. *J Med Chem* **2022,** *65* (6), 5134-5148.

13.   Seguí, P.; Aguilera-Correa, J. J.; Domínguez-Jurado, E.; Sánchez-López, C. M.; Pérez-Tanoira, R.; Ocaña, A. V.; Castro-Osma, J. A.; Esteban, J.; Marcilla, A.; Alonso-Moreno, C.; Pérez-Martínez, F. C.; Molina-Alarcón, M., A novel bis(pyrazolyl)methane compound as a potential agent against Gram-positive bacteria. *Sci Rep* **2021,** *11* (1), 16306.

14.   Teixeira, R. G.; Belisario, D. C.; Fontrodona, X.; Romero, I.; Tomaz, A. I.; Garcia, M. H.; Riganti, C.; Valente, A., Unprecedented collateral sensitivity for cisplatin-resistant lung cancer cells presented by new ruthenium organometallic compounds. *Inorganic Chemistry Frontiers* **2021,** *8* (8), 1983-1996.

15.   Lenis-Rojas, O. A.; Roma-Rodrigues, C.; Fernandes, A. R.; Carvalho, A.; Cordeiro, S.; Guerra-Varela, J.; Sánchez, L.; Vázquez-García, D.; López-Torres, M.; Fernández, A.; Fernández, J. J., Evaluation of the In Vitro and In Vivo Efficacy of Ruthenium Polypyridyl Compounds against Breast Cancer. *International journal of molecular sciences* **2021,** *22* (16).

16.   Suárez-Ortiz, G. A.; Hernández-Correa, R.; Morales-Moreno, M. D.; Toscano, R. A.; Ramirez-Apan, M. T.; Hernandez-Garcia, A.; Amézquita-Valencia, M.; Araiza-Olivera, D., Diastereomeric Separation of Chiral fac-Tricarbonyl(iminopyridine) Rhenium(I) Complexes and Their Cytotoxicity

Studies: Approach toward an Action Mechanism against Glioblastoma. *Journal of Medicinal Chemistry* **2022,** *65* (13), 9281-9294.

17.	Schindler, K.; Zobi, F., Anticancer and Antibiotic Rhenium Tri- and Dicarbonyl Complexes: Current Research and Future Perspectives. *Molecules* **2022,** *27* (2), 539.

18.	Knopf, K. M.; Murphy, B. L.; MacMillan, S. N.; Baskin, J. M.; Barr, M. P.; Boros, E.; Wilson, J. J., In Vitro Anticancer Activity and in Vivo Biodistribution of Rhenium(I) Tricarbonyl Aqua Complexes. *Journal of the American Chemical Society* **2017,** *139* (40), 14302-14314.

19.	Collery, P.; Bastian, G.; Santoni, F.; Mohsen, A.; Wei, M.; Collery, T.; Tomas, A.; Desmaele, D.; D'Angelo, J., Uptake and efflux of rhenium in cells exposed to rhenium diseleno-ether and tissue distribution of rhenium and selenium after rhenium diseleno-ether treatment in mice. *Anticancer research* **2014,** *34* (4), 1679-89.

20.	Collery, P.; Mohsen, A.; Kermagoret, A.; Corre, S.; Bastian, G.; Tomas, A.; Wei, M.; Santoni, F.; Guerra, N.; Desmaële, D.; d'Angelo, J., Antitumor activity of a rhenium (I)-diselenoether complex in experimental models of human breast cancer. *Investigational new drugs* **2015,** *33* (4), 848-60.

21.	King, A. P.; Marker, S. C.; Swanda, R. V.; Woods, J. J.; Qian, S.-B.; Wilson, J. J., A Rhenium Isonitrile Complex Induces Unfolded Protein Response-Mediated Apoptosis in Cancer Cells. *Chemistry – A European Journal* **2019,** *25* (39), 9206-9210.

22.	Simpson, P. V.; Casari, I.; Paternoster, S.; Skelton, B. W.; Falasca, M.; Massi, M., Defining the Anti-Cancer Activity of Tricarbonyl Rhenium Complexes: Induction of G2/M Cell Cycle Arrest and Blockade of Aurora-A Kinase Phosphorylation. *Chemistry* **2017,** *23* (27), 6518-6521.

23.	Maier, A. S.; Thomas, C.; Kränzlein, M.; Pehl, T. M.; Rieger, B., Macromolecular Rhenium–Ruthenium Complexes for Photocatalytic CO2 Conversion: From Catalytic Lewis Pair Polymerization to Well-Defined Poly(vinyl bipyridine)–Metal Complexes. *Macromolecules* **2022,** *55* (16), 7039-7048.

24.	Kaur, M.; Kapila, A.; Yempally, V.; Kaur, H., Synthesis, structural elucidation, and catalytic activity of bimetallic rhenium-tin complexes containing Schiff base ligand. *Journal of Molecular Structure* **2022,** *1249*, 131545.

25.	Mkhatshwa, M.; Moremi, J. M.; Makgopa, K.; Manicum, A.-L. E., Nanoparticles Functionalised with Re(I) Tricarbonyl Complexes for Cancer Theranostics. *International journal of molecular sciences* **2021,** *22* (12), 6546.

26.	Schanne, G.; Henry, L.; Ong, H. C.; Somogyi, A.; Medjoubi, K.; Delsuc, N.; Policar, C.; García, F.; Bertrand, H. C., Rhenium carbonyl complexes bearing methylated triphenylphosphonium cations as antibody-free mitochondria trackers for X-ray fluorescence imaging. *Inorganic Chemistry Frontiers* **2021,** *8* (16), 3905-3915.

27.	Case, D. R.; Spear, A.; Henwood, A. F.; Nanao, M.; Dampf, S.; Korter, T. M.; Gunnlaugsson, T.; Zubieta, J.; Doyle, R. P., [Re(CO)3(5-PAN)Cl], a rhenium(i) naphthalimide complex for the visible light photocatalytic reduction of CO2. *Dalton Transactions* **2021,** *50* (10), 3479-3486.

28.	Álvarez, D.; Menéndez, M. I.; López, R., Computational Design of Rhenium(I) Carbonyl Complexes for Anticancer Photodynamic Therapy. *Inorganic chemistry* **2022,** *61* (1), 439-455.

29.	Pete, S.; Roy, N.; Kar, B.; Paira, P., Construction of homo and heteronuclear Ru(II), Ir(III) and Re(I) complexes for target specific cancer therapy. *Coordination Chemistry Reviews* **2022,** *460*, 214462.

30.	Li, Z.-Y.; Shen, Q.-H.; Mao, Z.-W.; Tan, C.-P., Rising Interest in the Development of Metal Complexes in Cancer Immunotherapy. *Chemistry – An Asian Journal* **2022,** *17* (13), e202200270.

31.	Asadian, S.; Piryaei, A.; Gheibi, N.; Aziz Kalantari, B.; Reza Davarpanah, M.; Azad, M.; Kapustina, V.; Alikhani, M.; Moghbeli Nejad, S.; Keshavarz Alikhani, H.; Mohamadi, M.; Shpichka, A.; Timashev, P.; Hassan, M.; Vosough, M., Rhenium Perrhenate ((188)ReO(4)) Induced Apoptosis and Reduced Cancerous Phenotype in Liver Cancer Cells. *Cells* **2022,** *11* (2).

32.	Rigaku, O. *CrysAlis PRO Software system*, Rigaku Corporation: Oxford, UK, 2018.

33.   Sheldrick, G., SHELXT - Integrated space-group and crystal-structure determination. *Acta Crystallographica Section A* **2015,** *71* (1), 3-8.

34.   Chai, J.-D.; Head-Gordon, M., Long-range corrected hybrid density functionals with damped atom–atom dispersion corrections. *Physical Chemistry Chemical Physics* **2008,** *10* (44), 6615-6620.

35.   Grimme, S., Semiempirical GGA-type density functional constructed with a long-range dispersion correction. *Journal of Computational Chemistry* **2006,** *27* (15), 1787-1799.

36.   Singla, P.; Riyaz, M.; Singhal, S.; Goel, N., Theoretical study of adsorption of amino acids on graphene and BN sheet in gas and aqueous phase with empirical DFT dispersion correction. *Physical Chemistry Chemical Physics* **2016,** *18* (7), 5597-5604.

37.   Steinmann, S. N.; Csonka, G.; Corminboeuf, C., Unified Inter- and Intramolecular Dispersion Correction Formula for Generalized Gradient Approximation Density Functional Theory. *J Chem Theory Comput* **2009,** *5* (11), 2950-8.

38.   Humphrey, W.; Dalke, A.; Schulten, K., VMD: visual molecular dynamics. *J Mol Graph* **1996,** *14* (1), 33-8, 27-8.

39.   Spackman, P. R.; Turner, M. J.; McKinnon, J. J.; Wolff, S. K.; Grimwood, D. J.; Jayatilaka, D.; Spackman, M. A., CrystalExplorer: a program for Hirshfeld surface analysis, visualization and quantitative analysis of molecular crystals. *Journal of applied crystallography* **2021,** *54* (Pt 3), 1006-1011.

40.   Lu, T.; Chen, F., Multiwfn: A multifunctional wavefunction analyzer. *Journal of Computational Chemistry* **2012,** *33* (5), 580-592.

41.   Manicum, A.; Schutte-Smith, M.; Kemp, G.; Visser, H. G., Illustration of the electronic influence of coordinated β-diketone type ligands: A kinetic and structural study. *Polyhedron* **2015,** *85*, 190-195.

42.   Manicum, A.-L. E.; Schutte-Smith, M.; Alexander, O. T.; Twigge, L.; Roodt, A.; Visser, H. G., First kinetic data of the CO substitution in fac-[Re(L,L'-Bid)(CO)3(X)] complexes (L,L'-Bid = acacetylacetonate or tropolonate) by tertiary phosphines PTA and PPh3: Synthesis and crystal structures of water-soluble rhenium(I) tri- and dicarbonyl complexes with 1,3,5-triaza-7-phosphaadamantane (PTA). *Inorganic Chemistry Communications* **2019,** *101*, 93-98.

43.   Manicum, A.-L. E.; Schutte-Smith, M.; Visser, H. G., The synthesis and structural comparison of fac-[Re(CO)3]+ containing complexes with altered β-diketone and phosphine ligands. *Polyhedron* **2018,** *145*, 80-87.

44.   Manicum, A.-L.; Alexander, O.; Schutte-Smith, M.; Visser, H. G., Synthesis, characterization and substitution reactions of fac-[Re(O,O'-bid)(CO)3(P)] complexes, using the "2+1" mixed ligand model. *Journal of Molecular Structure* **2020,** *1209*, 127953.

45.   Manicum, A.-L. E.; Schutte-Smith, M.; Malan, F. P.; Visser, H. G., Steric and electronic influence of Re(I) tricarbonyl complexes with various coordinated β-diketones. *Journal of Molecular Structure* **2022,** *1264*, 133278.

46.   Benny, P. D.; Ganguly, T.; Raiford, L.; Fugate, G. A.; Twamley, B., Synthesis and reactivity of acetylacetone with amine ligands in fac-Re(OH2)3(CO)3+ complexes. *Inorganic Chemistry Communications* **2011,** *14* (2), 392-395.

47.   Benny, P. D.; Fugate, G. A.; Ganguly, T.; Twamley, B.; Bučar, D.-K.; MacGillivray, L. R., Unusual reactivity of acetylacetone with imidazole/histamine complexes and fac-M(OH2)3(CO)3+ (M=Re, 99mTc). *Inorganica Chimica Acta* **2011,** *365* (1), 356-362.

48.   Manicum, A.-L.; Alexander, O.; Schutte-Smith, M.; Visser, H. G., Crystal structure of fac-(acetylacetonato-κ2O,O')tricarbonyl(tri-m-tolyl phosphane-κP)rhenium(I), C29H28O5PRe. *Zeitschrift für Kristallographie - New Crystal Structures* **2018,** *233* (1), 23-25.

49.   Manicum, A.-L.; Alexander, O.; Schutte-Smith, M.; Visser, H. G.; Roodt, A., Crystal structure of fac-(acetylacetonato-κ2O,O')tricarbonyl(benzyldiphenylphosphine-κP)rhenium(I), C27H24O5PRe. *Zeitschrift für Kristallographie - New Crystal Structures* **2017,** *232* (6), 957-959.

50.   Manicum, A.-L.; Schutte-Smith, M.; Visser, H. G., Crystal structure of fac-(acetylacetonato-κ2O,O')tricarbonyl(tri(p-tolyl)phosphine-κP)rhenium(I), C29H28O5PRe. *Zeitschrift für Kristallographie - New Crystal Structures* **2017,** *232* (6), 951-955.

51.   Manicum, A.-L.; Schutte-Smith, M.; Visser, H. G., Journal: Zeitschrift für Kristallographie-New Crystal Structures, 2017, № 6, p. 951-955. *Zeitschrift für Kristallographie-New Crystal Structures* **2017,** (6), 951-955.

52.   Louis, H.; Mathias, G. E.; Unimuke, T. O.; Emori, W.; Ling, L.; Owen, A. E.; Adeyinka, A. S.; Ntui, T. N.; Cheng, C.-R., Isolation, characterization, molecular electronic structure investigation, and in-silico modeling of the anti-inflammatory potency of trihydroxystilbene. *Journal of Molecular Structure* **2022,** *1266*, 133418.

53.   Doust Mohammadi, M.; Abdullah, H. Y.; Louis, H.; Mathias, G. E., 2D boron nitride material as a sensor for H2SiCl2. *Computational and Theoretical Chemistry* **2022,** *1213*, 113742.

54.   Bassey, V. M.; Apebende, C. G.; Idante, P. S.; Louis, H.; Emori, W.; Cheng, C.-R.; Agwupuye, J. A.; Unimuke, T. O.; Wei, K.; Asogwa, F. C., Vibrational Characterization and Molecular Electronic Investigations of 2-acetyl-5-methylfuran using FT-IR, FT-Raman, UV-VIS, NMR, and DFT Methods. *J Fluoresc* **2022,** *32* (3), 1005-1017.

55.   Demir, P.; Akman, F., Molecular structure, spectroscopic characterization, HOMO and LUMO analysis of PU and PCL grafted onto PEMA-co-PHEMA with DFT quantum chemical calculations. *Journal of Molecular Structure* **2017,** *1134*, 404-415.

56.   Fedorov, D. G.; Ishida, T.; Kitaura, K., Multilayer Formulation of the Fragment Molecular Orbital Method (FMO). *The Journal of Physical Chemistry A* **2005,** *109* (11), 2638-2646.

57.   List, N. H.; Curutchet, C.; Knecht, S.; Mennucci, B.; Kongsted, J., Toward Reliable Prediction of the Energy Ladder in Multichromophoric Systems: A Benchmark Study on the FMO Light-Harvesting Complex. *Journal of Chemical Theory and Computation* **2013,** *9* (11), 4928-4938.

58.   Rakhi, R.; Suresh, C. H., A DFT study on dihydropyrazine annulated linear polyacenes: aromaticity, stability and HOMO–LUMO energy modulation. *Physical Chemistry Chemical Physics* **2016,** *18* (35), 24631-24641.

59.   Louis, H.; Mathias, G. E.; Ikenyirimba, O. J.; Unimuke, T. O.; Etiese, D.; Adeyinka, A. S., Metal-Doped Al12N12X (X = Na, Mg, K) Nanoclusters as Nanosensors for Carboplatin: Insight from First-Principles Computation. *The Journal of Physical Chemistry B* **2022,** *126* (27), 5066-5080.

60.   Zade, S. S.; Bendikov, M., From oligomers to polymer: convergence in the HOMO-LUMO gaps of conjugated oligomers. *Org Lett* **2006,** *8* (23), 5243-6.

61.   Ahmadi Peyghan, A.; Hadipour, N. L.; Bagheri, Z., Effects of Al Doping and Double-Antisite Defect on the Adsorption of HCN on a BC2N Nanotube: Density Functional Theory Studies. *The Journal of Physical Chemistry C* **2013,** *117* (5), 2427-2432.

62.   Gber, T. E.; Louis, H.; Owen, A. E.; Etinwa, B. E.; Benjamin, I.; Asogwa, F. C.; Orosun, M. M.; Eno, E. A., Heteroatoms (Si, B, N, and P) doped 2D monolayer MoS2 for NH3 gas detection. *RSC Advances* **2022,** *12* (40), 25992-26010.

63.   Osigbemhe, I. G.; Oyoita, E. E.; Louis, H.; Khan, E. M.; Etim, E. E.; Edet, H. O.; Ikenyirimba, O. J.; Oviawe, A. P.; Obuye, F., Antibacterial potential of N-(2-furylmethylidene)-1, 3, 4-thiadiazole-2-amine: Experimental and theoretical investigations. *Journal of the Indian Chemical Society* **2022,** *99* (9), 100597.

64.   Mohammadi, M. D.; Abbas, F.; Louis, H.; Mathias, G. E.; Unimuke, T. O., Trapping of CO, CO2, H2S, NH3, NO, NO2, and SO2 by polyoxometalate compound. *Computational and Theoretical Chemistry* **2022,** *1215*, 113826.

65.   Unimuke, T. O.; Louis, H.; Eno, E. A.; Agwamba, E. C.; Adeyinka, A. S., Meta-Hybrid Density Functional Theory Prediction of the Reactivity, Stability, and IGM of Azepane, Oxepane, Thiepane, and Halogenated Cycloheptane. *ACS Omega* **2022,** *7* (16), 13704-13720.

66.	Kumar, M.; Kariem, M.; Sheikh, H. N.; Frontera, A.; Seth, S. K.; Jassal, A. K., A series of 3D lanthanide coordination polymers decorated with a rigid 3,5-pyridinedicarboxylic acid linker: syntheses, structural diversity, DFT study, Hirshfeld surface analysis, luminescence and magnetic properties. *Dalton Transactions* **2018,** *47* (35), 12318-12336.

67.	Seth, S. K.; Bauzá, A.; Frontera, A., Screening polymorphism in a Ni(ii) metal–organic framework: experimental observations, Hirshfeld surface analyses and DFT studies. *CrystEngComm* **2018,** *20* (6), 746-754.

68.	Ashfaq, M.; Tahir, M. N.; Muhammad, S.; Munawar, K. S.; Ali, A.; Bogdanov, G.; Alarfaji, S. S., Single-Crystal Investigation, Hirshfeld Surface Analysis, and DFT Study of Third-Order NLO Properties of Unsymmetrical Acyl Thiourea Derivatives. *ACS Omega* **2021,** *6* (46), 31211-31225.

69.	Mahmoudi, G.; Bauzá, A.; Rodríguez-Diéguez, A.; Garczarek, P.; Kaminsky, W.; Frontera, A., Synthesis, X-ray characterization, DFT calculations and Hirshfeld surface analysis studies of carbohydrazone based on Zn(ii) complexes. *CrystEngComm* **2016,** *18* (1), 102-112.

70.	Ashfaq, M.; Munawar, K. S.; Tahir, M. N.; Dege, N.; Yaman, M.; Muhammad, S.; Alarfaji, S. S.; Kargar, H.; Arshad, M. U., Synthesis, Crystal Structure, Hirshfeld Surface Analysis, and Computational Study of a Novel Organic Salt Obtained from Benzylamine and an Acidic Component. *ACS Omega* **2021,** *6* (34), 22357-22366.

71.	Estévez, L.; Queizán, M.; Mosquera, R. A.; Guidi, L.; Lo Piccolo, E.; Landi, M., First Characterization of the Formation of Anthocyanin–Ge and Anthocyanin–B Complexes through UV–Vis Spectroscopy and Density Functional Theory Quantum Chemical Calculations. *Journal of Agricultural and Food Chemistry* **2021,** *69* (4), 1272-1282.

72.	Eiler, S.; Gangloff, M.; Duclaud, S.; Moras, D.; Ruff, M., Overexpression, purification, and crystal structure of native ER alpha LBD. *Protein Expr Purif* **2001,** *22* (2), 165-73.

73.	Mazumdar, M.; Fournier, D.; Zhu, D. W.; Cadot, C.; Poirier, D.; Lin, S. X., Binary and ternary crystal structure analyses of a novel inhibitor with 17beta-HSD type 1: a lead compound for breast cancer therapy. *Biochem J* **2009,** *424* (3), 357-66.

74.	Dutertre, M.; Smith, C. L., Ligand-independent interactions of p160/steroid receptor coactivators and CREB-binding protein (CBP) with estrogen receptor-alpha: regulation by phosphorylation sites in the A/B region depends on other receptor domains. *Mol Endocrinol* **2003,** *17* (7), 1296-314.

75.	De Paula, V. S.; Gomes, N. S.; Lima, L. G.; Miyamoto, C. A.; Monteiro, R. Q.; Almeida, F. C.; Valente, A. P., Structural basis for the interaction of human β-defensin 6 and its putative chemokine receptor CCR2 and breast cancer microvesicles. *Journal of molecular biology* **2013,** *425* (22), 4479-95.

76.	Maximov, P. Y.; Abderrahman, B.; Fanning, S. W.; Sengupta, S.; Fan, P.; Curpan, R. F.; Rincon, D. M. Q.; Greenland, J. A.; Rajan, S. S.; Greene, G. L.; Jordan, V. C., Endoxifen, 4-Hydroxytamoxifen and an Estrogenic Derivative Modulate Estrogen Receptor Complex Mediated Apoptosis in Breast Cancer. *Mol Pharmacol* **2018,** *94* (2), 812-822.

77.	Da Silva, H. C.; De Souza, L. A.; Dos Santos, H. F.; De Almeida, W. B., Determination of Anticancer Zn(II)–Rutin Complex Structures in Solution through Density Functional Theory Calculations of 1H NMR and UV–VIS Spectra. *ACS Omega* **2020,** *5* (6), 3030-3042.

78.	M. J. Frisch, G. W. Trucks, H. B. Schlegel, G. E. Scuseria, M. A. Robb, J. R. Cheeseman, G. Scalmani, V. Barone, B. Mennucci, G. A. Petersson, H. Nakatsuji, M. Caricato, X. Li, H. P. Hratchian, A. F. Izmaylov, J. Bloino, G. Zheng, J. L. Sonnenberg, M. Hada, M. Ehara, K. Toyota, R. Fukuda, J. Hasegawa, M. Ishida, T. Nakajima, Y. Honda, O. Kitao, H. Nakai, T. Vreven, J. A. Montgomery, Jr., J. E. Peralta, F. Ogliaro, M. Bearpark, J. J. Heyd, E. Brothers, K. N. Kudin, V. N. Staroverov, R. Kobayashi, J. Normand, K. Raghavachari, A. Rendell, J. C. Burant, S. S. Iyengar, J. Tomasi, M. Cossi, N. Rega, J. M. Millam, M. Klene, J. E. Knox, J. B. Cross, V. Bakken, C. Adamo, J. Jaramillo, R. Gomperts, R. E. Stratmann, O. Yazyev, A. J. Austin, R. Cammi, C. Pomelli, J. W. Ochterski, R. L. Martin, K. Morokuma, V. G. Zakrzewski, G. A. Voth, P. Salvador, J. J.

Dannenberg, S. Dapprich, A. D. Daniels, Ö. Farkas, J. B. Foresman, J. V. Ortiz, J. Cioslowski, and D. J. Fox, *Gaussian 09* (Gaussian, Inc., Wallingford CT, 2016).

79. Dennington, R., Keith, T. A., & Millam, J. M. (2016). GaussView 6.0. 16. *Semichem Inc.: Shawnee Mission, KS, USA*.

80. NBO Version 3.1, E. D. Glendening, A. E. Reed, J. E.

81. Biova, Dassault System, [Software Product name 1], [Software version 1]; [Software product name 2], San Diego: Dassult Systemes, [2021]

82. AutoDock 4.2 Morris, G. M., Huey, R., Lindstrom, W., Sanner, M. F., Belew, R. K., Goodsell, D. S. and Olson, A. J. (2009) Autodock4 and AutoDockTools4: automated docking with selective receptors flexibility.